西北工業大學

Undergraduate Graduation Design(Thesis) Management Manual

（2023）

Title Research on Physical Layer Security Transmission Based on Orthogonal Time Frequency Space Modulation

Major Electronics and Information Engineering

Name Zian Chen

Supervisor Qian Xu

Graduation time 2023/07

Abstract

Orthogonal time frequency space (OTFS) modulation technology is considered a solution to high-mobility communication scenarios in the 6th generation (6G). The basic principle of OTFS is to transform the fast time-varying channel response in the time-frequency (TF) domain into the sparse time-invariant channel response in the delay-Doppler (DD) domain. Different from the orthogonal frequency division multiplexing (OFDM) modulation, which is widely used in 4th generation (4G) and 5th generation (5G), OTFS can resist multipath and Doppler effect efficiently even in a very high-speed scenario such as 500km/h. And the security of information transmission also catches much attention in the high-mobility wireless communication scenario. Thus, physical layer security (PLS) is introduced to exchange confidential messages over wireless media in the presence of unauthorized eavesdroppers, independent of higher-level encryption. This thesis focuses on the research of PLS based on the OTFS modulation technology, to guarantee security in high-mobility communication scenarios. The overall structure of this thesis can be summarized as follows:

Firstly, this thesis briefly introduces the transmission characteristics of the wireless channel. Then, four equivalent different representations of the linear time-varying (LTV) channel and transformation relations in between are indicated. Moreover, a physical discrete-path model is introduced to describe the wireless channel more specifically.

Secondly, to solve the communication performance degradation issue of traditional OFDM in high-mobility scenarios, this thesis indicates the principle and transmission

scheme of the OTFS system. Then, the reduced Cyclic Prefix (CP) is introduced which shows a better performance and increases the spectrum efficiency in the OTFS system, compared with the traditional full CP. The input-output relations under various conditions in the different domains are derived, as well as the effective matrix for different pulse-shaping filters. Moreover, the equivalence between time domain zero forcing (ZF) equalization and the DD domain ZF equalization is proved, as well as the minimum mean-square error (MMSE) equalization.

Finally, to address the security concerns in high-mobility 6G communication scenarios, this thesis researches an singular value decomposition (SVD) secure precoding strategy based on the OTFS system, which rotates the information symbols and distorts the constellation at the eavesdroppers. Even if the eavesdroppers are assumed to know everything about the rotate OTFS (R-OTFS) transmission scheme, still they cannot recover the original information but a degraded version, which realizes the physical layer security.

Keywords: OTFS, Delay-Doppler, PLS, SVD, Precoding

Table of Contents

List of Abbreviations

Abbreviation	Full Name
OTFS	Orthogonal Time Frequency Space
6G	6th Generation Mobile Networks
TF	Time-Frequency
DD	Delay-Doppler
OFDM	Orthogonal Frequency Division Multiplexing
4G	4th Generation Mobile Networks
5G	5th Generation Mobile Networks
PLS	Physical Layer Security
LTV	Linear Time-Varying
FCP	Full Cyclic Prefix
RCP	Reduced Cyclic Prefix
SVD	Singular Value Decomposition
ISFFT	Inverse Symplectic Finite Fourier Transform
SFFT	Symplectic Finite Fourier Transform
CSI	Channel Status Information
OSI	Open System Interconnection
MP	Message Passing
CP	Cyclic Prefix
GAMP	Generalized Approximate Message Passing

MIMO	Multiple Input Multiple Output
IM	Index Modulation
AI	Artificial Noise
ZF	Zero Forcing
MMSE	Minimum Mean-Square Error
ICI	Inter-carrier Interfernce
ISI	Inter-symbol Interfernce
IDI	Inter-Doppler Interfernce
TDD	Time Division Duplex
R-OTFS	Rotate OTFS
AWGN	Additive White Gaussian Noise
SNR	Signa- to-noise Ratio
SINR	Signal-to-interference-plus-noise Ratio
BER	Bit Error Rate
EVA	LTE-Extended Vehicular A model

List of Figures

Chapter One Introduction

In this chapter, the research background and significance of our research will be introduced. Then, the current research status at home and abroad are reviewed. The major work and chapter arrangements of this thesis are shown at the end of this chapter.

1.1 Research Background and Significance

With the rapid development of high-speed traffic, solving the problem of information transmission in the future high-speed scene has become a main research objective of 6th generation (6G) communication technology[1-6]. The main problem in the high-mobility channel is the fast time-varying fading. Because the high speed leads to high Doppler shift and expansion which seriously affects the performance of communication systems[7-9]. To solve the problems above, orthogonal time frequency space (OTFS) modulation technology is becoming a new solution.

Different from the traditional orthogonal frequency division multiplexing (OFDM) modulation, OTFS modulates information symbols onto a set of two-dimensional orthogonal basis functions in the Delay-Doppler (DD) domain[10]. Particularly, every information symbol in the DD domain is transmitted in all subcarriers and all time slots by inverse symplectic finite Fourier transform (ISFFT) and symplectic finite Fourier transform (SFFT), which means every symbol will experience almost the same constant fading[11-13]. Therefore, OTFS modulation converts the time-varying channel in the TF domain into the time-invariant impulse response in the DD domain, and then the system obtains a constant channel gain[14-16]. In addition, the DD domain also simplifies the required channel estimation and signal detection. OTFS has the potential to achieve full channel diversity, and effectively resist the negative impacts of the Doppler effect and multipath effect, to realize reliable transmission in high-mobility scenarios.

In modern wireless communication scenarios, the wireless channel is vulnerable to eavesdropping by some unauthorized illegal users due to its open feature, causing the leakage of private information. The traditional method to achieve communication security is encryption by using the secret key in the network layer to resist eavesdropping, that is in the high layer of communication network protocol framework, the plaintext is converted into ciphertext by secret key for secure transmission. In this case, it's hard for eavesdroppers to recover the original plaintext information accurately in a short time without the secret key. The security level of this cryptography-based encryption depends on the complexity of key cracking. However, with the continuous innovation of computer technology, its security has been greatly challenged[17].

Therefore, physical layer security (PLS) technology is introduced to supplement the upper layer encryption technology, which utilizes the superiority of channel status information (CSI) of the legitimate link. Generally, PLS mainly includes two research directions, which are the PLS transmission technology based on eavesdropping encoding and physical layer key generation technology based on channel variations. In reference [18], the position of PLS in the open system interconnection (OSI) reference model is shown in Figure 1.

To satisfy the high-mobility and security requests of the future communication scenario in 6G, it's necessary to research the PLS transmission strategy in the OTFS system, which is exactly the purpose of this thesis.

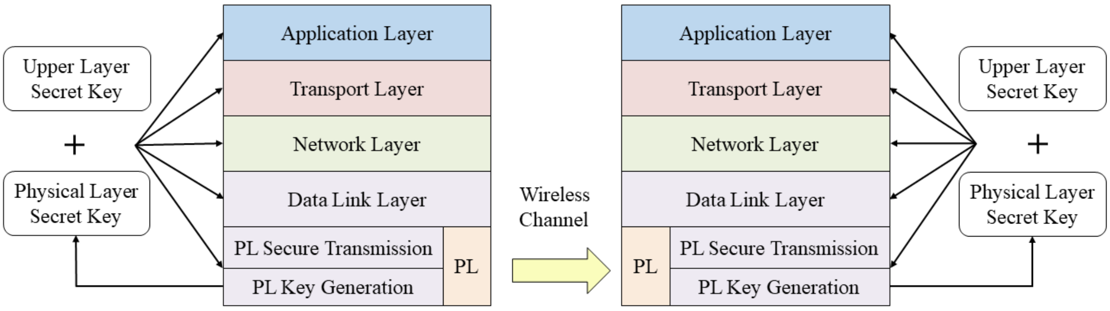

Figure 1 PLS in OSI reference model.

1.2 Current Research Status at Home and Abroad

1.2.1 Orthogonal Time Frequency Space Modulation

The OTFS system was first proposed by Hadani as a scheme to deal with time-varying channels in reference [19]. The system introduced the delay-Doppler domain, then modulated and demodulated the signal in this domain to meet the requirement of high Doppler shift. Simulation results in reference [20] showed that, compared with OFDM systems, OTFS systems had at least several dB gains more in the same channel conditions. Raviteja et al. analyzed the linear input and output vector model of the OTFS system in detail in reference [21], simplified the input-output relationship under integer Doppler shift, and demonstrated in detail the interference expression when the rectangular filter was used in reality. At the same time, they also proved that there is only Doppler interference in the OTFS system under the ideal biorthogonal waveform. Based on this vector model, a low complexity nonlinear iterative detection algorithm, namely message passing (MP) algorithm, was designed. Their simulation data showed that OTFS still has good performance without Cyclic Prefix (CP) overhead. Reference [22] studied and analyzed the principle and system model of OTFS technology modulation and demodulation, and then compared and analyzed the message passing algorithm and the generalized approximate message passing (GAMP) algorithm.

Reference [23] proposed a block-based OTFS receiver. which used the sparsity of channel matrix to realize the fast convergence through a channel equalizer based on least squares minimum residual and an iterative strategy between the symbol detector and the interference suppressor. Reference [24] proposed a multiplex scheduling scheme of OTFS and OFDM. Low mobility users used the OFDM system, while high mobility users used the OTFS system, to improve resource utilization and message transmission rate. Reference [25] proposed a cross-domain iterative detection algorithm. The algorithm applied the basic estimation and detection methods to the time domain and the time delay Doppler domain respectively, and iteratively updated the external information of the two domains through unitary transformation, thus making full use of the time domain channel sparsity and the time delay Doppler domain symbol constellation constraints.

In recent years, the research of OTFS has expanded from SISO scenarios to the multiple input multiple output (MIMO) scenarios, the system performance of OTFS was supposed to be improved by MIMO channel estimation and signal detection algorithm optimization. Reference [26] studied the system vector expression of OTFS-MIMO, and proposed the channel estimation and signal detection methods of OTFS-MIMO. Reference [27] used the vectorization formula to equivalent the channel matrix, and proposed a low-complexity OTFS-MIMO signal detection algorithm based on Markov chain Monte Carlo sampling and a channel estimation scheme based on the delay Doppler domain. The simulation results showed that OTFS outperformed OFDM in high-speed mobile scenarios. Reference [28] studied the precoding schemes for the

MIMO-OTFS system based on codebook, and singular value decomposition (SVD), and then modified the MRC detector. To obtain the spatial diversity, reference [29] introduced the index modulation (IM) to the MIMO-OTFS systems and proposed a system model and a low complexity signal detection method based on MIMO-OTFS-IM technologies. In reference [30], a dynamic grid resource allocation method for uplink in the OTFS system is proposed. By rationally arranging the resource allocation of pilots, guard intervals, and data symbols, the error performance is close to the traditional method achieved. However, the dynamic grid resource allocation method can send more data and improve resource utilization.

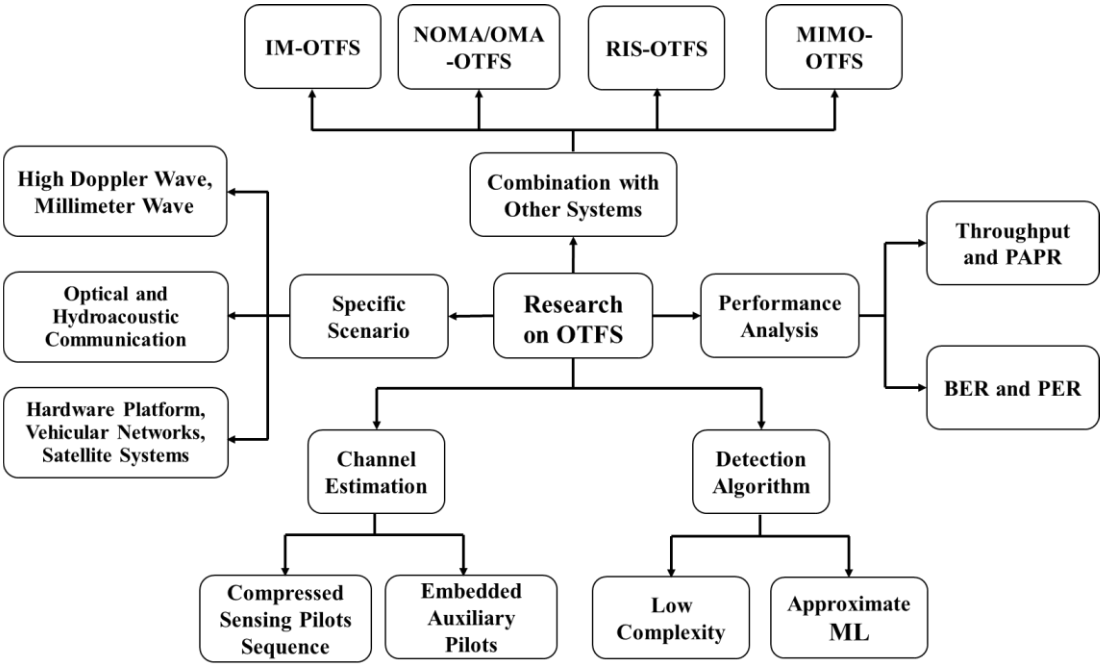

Figure 2 Research status of OTFS.

As shown in Figure 2, the present research on OTFS technology[9] is still not complete yet, and the future OTFS technology is expected to become an effective solution to high-speed mobile communication scenarios.

1.2.2 Physical Layer Security

In recent years, some new technologies have emerged in the field of wireless communication, such as large-scale antennae, millimeter wave communication, UAV communication, and so on. For the PLS transmission in large-scale antennae, reference [31] studied the reachable private rate and security interrupt probability in large-scale antenna relay systems. In the research on the application of multi-antenna in PLS, Artificial noise injection and secure pre-coding are often used in combination. In the MISO channel, reference [32] analyzed the PLS when the eavesdroppers are distributed randomly and proposed a throughput optimization scheme assisted by artificial noise (AI). In the case of incomplete CSI, reference [33] considered the existence of passive eavesdroppers and the existence of multi-user secure communication based on the zero forcing (ZF) precoder and minimum mean-square error (MMSE) precoder. Reference [34] used directional modulation to enhance physical layer transport security. Reference [35] used the statistical channel model to analyze the impact of the density of obstacles and eavesdroppers in random networks on the security outage probability of millimeter wave communication systems.

The research on physical layer security transmission in the UAV communication scenario included optimizing the flight path in the relay system to maximize the average privacy rate [36], optimizing the hover height to maximize the privacy rate in reference [37], and optimizing the launch power to maximize the sum privacy rate in reference [38]. These emerging technologies have injected new vitality into the physical layer security transmission. Reference [39] studied the maximization of the security energy efficiency of the relay system in the presence of potential eavesdroppers, and the path optimization when the location of the eavesdropper is not completely determined. Reference [40] further extended it by proposing a scenario of cooperative multi-UAV-assisted secure communication and investigating a cooperative jamming strategy, in which one node was deployed as a relay to assist ground users in information interaction, but there were additional ground eavesdroppers in the process, when another node send artificial jamming noise to ground eavesdroppers to counteract eavesdropping, and the authors investigated the cooperative path optimization design of two UAVs in the air to enable the whole UAV communication system to communicate securely. The goal of Reference [41] was to maximize the security rate in the worst case by jointly optimizing the trajectory and transmission power under the coexistence of multiple eavesdroppers, considering the energy consumption in this scenario. Reference [42] combined UAV with a millimeter wave network and studied the security communication problem as an active friendly jammer in a millimeter wave network to assist the safe transmission of the system. These emerging technologies have injected new vitality into the physical layer security.

1.3 The Major Work and Chapter Arrangement

To solve the high-mobility and security problems in the 6G communication scenario, this thesis mainly research the OTFS modulation technology and researches a secure precoding strategy in the OTFS system.

The chapter arrangements are as follows:

In chapter one, the research background and significance of our research are first indicated. Then the current research status at home and abroad are reviewed. The major work and the chapter arrangements of this thesis are shown as follow:

In chapter two, the wireless transmission characteristics are classified into several channel fading types. Then, four equivalent different functions are shown to represent the linear time-varying (LTV) channel and the transformation relations in between. The physical discrete-path model is introduced to describe the physical wireless channel more specifically.

In chapter three, the OTFS system model is introduced from the transmitter to the receiver. The reduced CP is compared with the traditional full CP. to study the spectrum efficiency of the OTFS system. Then from the aspect of the transceiver waveform types, three different conditions are assumed, which are the arbitrary waveforms, the ideal pulses satisfying the bi-orthogonal property, and the rectangular pulses used in practical. In the above three conditions, the input-output relations in the TF domain and DD domain are derived. Moreover, the inter-carrier interference (ICI) and inter-symbol interference (ISI) in the TF domain and inter-Doppler interference (IDI) in the DD domain are analyzed. With the effective channel matrix derived in the input-output relations, the equivalence between time domain ZF equalization and the DD domain ZF equalization is proved, as well as the MMSE equalization.

In chapter four, the principle of the SVD is first introduced. Then, a secure precoding strategy is researched based on SVD in the OTFS system, which uses no secret key but the superiority of the legitimate channel to realize PLS. Because of the reciprocity of the wireless channel in the time division duplex (TDD) system, both and only the legitimate transceivers can extract the effective channel matrix from the legitimate channel CSI. Then the extracted effective channel matrix will be decomposed by the SVD method to get the matrices, which are used to generate the rotate OTFS (R-OTFS) waveform by precoding. Due to the differences and independence of physical channels, those eavesdroppers can not obtain the correct information, even if they know all of the R-OTFS, which finally guarantees the security of private information in the high-mobility OTFS system.

In chapter five, the summary and prospect are given, where the research content of the thesis is summarized, and a prospect is made for the applications of PLS in the high-mobility OTFS systems.

Chapter Two Wireless Channel

In this chapter, the wireless channel, including the classification of the channel fading types, the representations of the LTV channel in different domains, and the physical discrete-path model are introduced.

2.1 Wireless Channel Transmission Characteristics

In wireless communication systems, signals are transmitted in the form of electromagnetic waves from the transmitters to the receivers through wireless channels. In the process of propagation, electromagnetic waves will be affected by the reflection, scattering, and diffraction of obstacles in the wireless channels, which changes the amplitudes, frequencies, and time of the transmitted signals due to the wireless channel transmission characteristics. Thus a power loss and a decline in communication performance are caused during the transmission process.

2.1.1 Classification of Wireless Channel Fading

From the perspective of distance, the classification of the wireless channel fading is shown in Figure 3. Wireless channel fading can be generally divided into large-scale fading and small-scale fading. Large-scale fading includes path loss during the propagation of electromagnetic waves and the shadow effect caused by the occlusion of large obstacles[43]. Small-scale fading is characterized by drastic changes in signal power over short distances (order of wavelength), including the frequency-selective fading caused by the multipath effect and the time-selective fading caused by the Doppler effect[44,45].

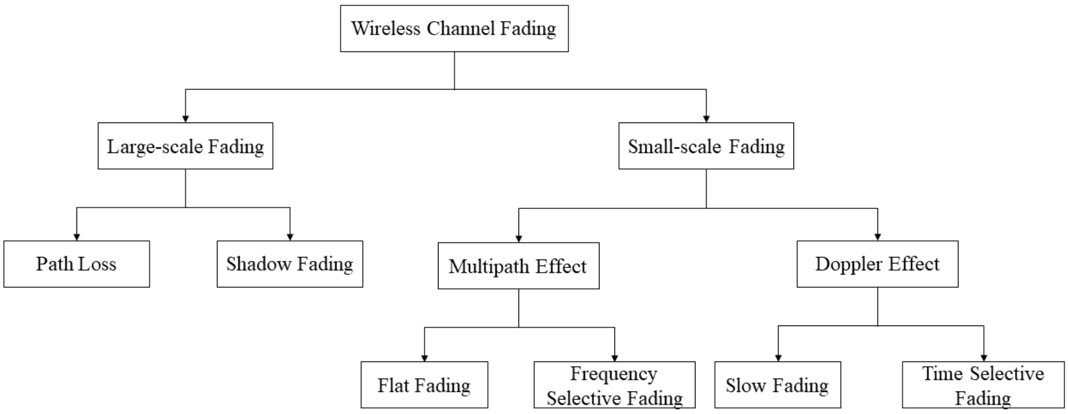

Figure 3 Classification of wireless channel fading.

2.1.2 Path Loss and Shadow Fading

Path loss is caused by the radiative diffusion of transmitted power and the propagation characteristics of the wireless channel itself. This phenomenon leads to the change of the received power of the signal over a long distance (100m~1000m).

Shadow fading is due to the presence of obstacles over a medium distance (hundreds of wavelengths), leading to the attenuation of the signal power, or even blocking the signal. Path loss and shadow fading cause signal power attenuation in large-scale distance transmission, which is also called large-scale attenuation[46].

2.1.3 Multipath Effect and Frequency-selective Fading

In the practical wireless channels, due to the presence of scatterers, the transmitted signals will go through different degrees of attenuation in different paths and finally superimpose at the receiver. This phenomenon is called the multipath effect, which will cause delay spread shown in Figure 4. The different lengths of multiple propagation paths from the transmitter to the receiver also result in different delays of the transmitted signals[47]. Such channels are called time-dispersive channels. The delay difference between the two paths in Figure 4 is given by

$$\Delta\tau = \frac{r_2 + r_3}{c} - \frac{r_1}{c}, \tag{2-1}$$

where c represents the speed of light.

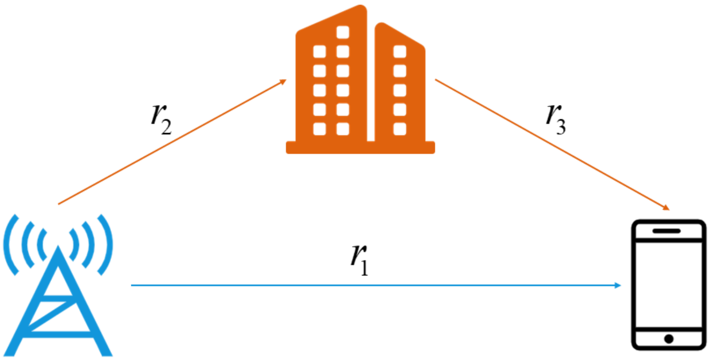

Figure 4 Time spread schematic diagram.

The delay power spectrum denoted as $P(\tau)$ is the most important parameter to describe the bandwidth characteristics, which represents the average power of the given multipath delays. $P(\tau)$ is usually obtained by broadband channel measurements in the time domain or in the time-frequency (TF) domain[48]. $P(\tau)$ can be calculated by the local channel impulse response in the time domain

$$P(\tau) = \int_{-\infty}^{+\infty} |h(t,\tau)|^2 dt, \tag{2-2}$$

where τ represents the delay. $P(\tau)$ shows the power intensity of the received signal within the time range $[\tau, \tau + d\tau]$ when transmitting the unit energy pulse, which is irrelevant to the Doppler shift. Its actual range of integration is a quasi-static time interval.

The average delay $\bar{\tau}$ and root-mean-square (RMS) delay σ_T are both essential variables to describe the channel delay spread, which can be expressed as

$$\bar{\tau} = \frac{\int_0^{\infty} \tau P(\tau) d\tau}{\int_0^{\infty} P(\tau) d\tau}, \tag{2-3}$$

$$\sigma_\tau = \sqrt{\frac{\int_0^{\infty^2} (\tau - \bar{\tau})^2 P(\tau) d\tau}{\int_0^{\infty} P(\tau) d\tau}} . \tag{2-4}$$

The coherent bandwidth denoted as B_c represents the maximum frequency difference of the channel when the envelope correlation is a certain value. The RMS delay σ_τ can be used to estimate the coherent bandwidth B_c since they have an approximately inverse proportional relationship, which is $B_c \approx 1/\sigma_\tau$. When the signal bandwidth is far smaller than the coherent bandwidth, the amplitude of the channel response is a constant value within the bandwidth. In this case, the signal of all frequencies will go through similar flat fading, which is also called frequency non-selective fading. On the contrary, when the signal bandwidth is far larger than the coherent bandwidth, different frequency components in the signal will be affected by different channel responses, which is called frequency-selective fading. In this case, the transmitted signal will be severely distorted[49].

2.1.4 Doppler Effect and Time-selective Fading

In wireless communication, the signal frequencies will be shifted if the transmitter or receiver is moving relative to each other, which is called the Doppler shift. Figure 5 shows the Doppler shift in a high-mobility scenario. When they move towards, the frequencies of the received signal will be higher than the transmitted signal. When they move in opposite directions, the frequencies of the received signal will be lower than the transmitted signal. This is called the Doppler effect.

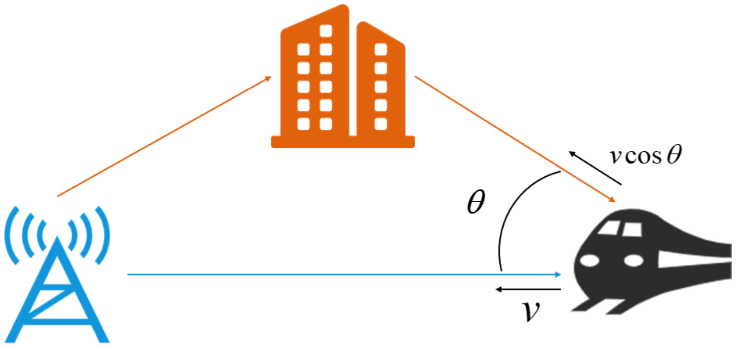

Figure 5 Doppler shift schematic diagram

For electromagnetic waves, the Doppler shift due to the Doppler effect depends on the relative speed, which can be expressed as

$$f_D = \frac{v}{\lambda}\cos\theta = f_c\frac{v}{c}\cos\theta\,, \tag{2-5}$$

where f_c is the carrier frequency, v is the relative speed, c is the speed of light, and θ is the angle between the relative moving direction and the electromagnetic wave incident direction. These parameters will directly affect the Doppler shift f_D, which means the faster the mobile terminal moves, the larger the Doppler shifts. When the incident angle is zero degrees, the Doppler shift reaches its maximum. Thus, the maximum Doppler shift is defined as

$$f_{D\max} = \frac{v}{\lambda} = f_c\frac{v}{c}\,. \tag{2-6}$$

In the process of radio wave transmission, the propagation mechanisms including scattering, diffraction and reflection, cause the multipath channel where the signal propagates in different directions. The multipath components cause the spread on the frequency spectrum of the received signal, which is called the Doppler spread.

Different incident angles produce different Doppler frequency shifts, and The superposition of all scattering components forms a continuous Doppler power spectrum. When the incident angle of the radio wave is uniformly distributed, which means multipath radio waves come uniformly from all directions, the incident angles of the received radio waves are uniformly distributed on $[0, 2\pi]$. The Doppler power spectrum in this case is called the classical Doppler power spectrum[48]. As shown in Figure 6, the classical Doppler power spectrum is centered at the carrier frequency f_c and distributed on $[f_c - f_{D\max}, f_c + f_{D\max}]$.

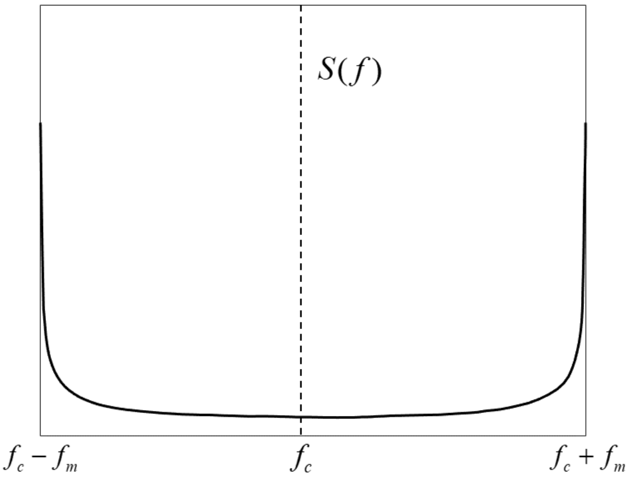

Figure 6 Classical Doppler power spectrum.

A time parameter corresponding to the Doppler spread is the coherent time denoted as T_c, which can be used to describe the frequency dispersion characteristics of time domain channels. Coherent time T_c has an approximately inversely proportional relationship with the maximum Doppler spread $f_{D\max}$, which can be written as

$$T_c \approx \frac{1}{f_{D\max}}, \tag{2-7}$$

Coherent time is defined as the statistical mean of the time intervals in which the channel impulse responses remain unchanged and the received signals have strong amplitude correlations. When the symbol duration denoted as T_s is less than the coherent time T_c, the channel characteristics do not change much during the signal transmission, which is called slow fading. When the symbol duration T_s is larger than the coherent time T_c, the channel characteristics have already changed a lot during the signal transmission, which is called fast fading or time-selective fading.

2.2 Representation of LTV Channel

The delay of the received signal is caused by channel multipath delay propagation and time spread, while the Doppler shift of the received signal is caused by the mobility of the transmitter or receiver and the oscillator drift. A deterministic linear time-varying (LTV) channel is modeled to derive the specific expressions of the received signal[50].

An LTV channel can be represented in four equivalent forms, which are time-varying impulse response $c(\tau,t)$, delay-Doppler spreading function (or delay-Doppler impulse response) $h(\tau,v)$, Doppler spreading function (or bi-frequency function) $C(f,v)$, and time-varying frequency response $H(f,t)$[51]. Each of these functions contains a complete description of the channel, which contains any two variables among time t, delay τ, frequency f, and Doppler frequency v. As shown in Figure 7[52], each function can be transformed to each other by doing several Fourier transforms (FT) denoted as $\mathcal{F}$ or inverse Fourier transforms (IFT) denoted as $\mathcal{F}^{-1}$. For example, the relationships between $c(\tau,t)$, $h(\tau,v)$, and $H(f,t)$ are given by

$$H(f,t)=\int c(\tau,t)e^{-j2\pi f\tau}d\tau\,, \tag{2-8}$$

$$h(\tau,v)=\int c(\tau,t)e^{-j2\pi vt}dt\,. \tag{2-9}$$

In particular, the transformation between $H(f,t)$ and $h(\tau,v)$ can be realized directly by ISFFT or SFFT, which can be expressed by

$$H(t,f)=\iint h(\tau,v)e^{j2\pi(vt-f\tau)}d\tau dv\,, \tag{2-10}$$

$$h(\tau,v)=\iint H(t,f)e^{-j2\pi(vt-f\tau)}dtdf\,. \tag{2-11}$$

Assume that $s(t)$ is the narrowband transmitted signal, and $r(t)$ is the received signal. Then the input-output relation in the time domain is given by

$$\begin{aligned} r(t) &= \int_0^{\tau_{\max}} c(\tau,t)s(t-\tau)d\tau \\ &= \int_{-\infty}^{+\infty} H(t,f)S(f)e^{j2\pi ft}df \\ &= \int_{-v_{\max}}^{v_{\max}} \int_0^{\tau_{\max}} h(\tau,v)s(t-\tau)e^{j2\pi v(t-\tau)}d\tau dv \end{aligned} , \tag{2-12}$$

where $\tau_{\max}$ denotes the maximum channel delay, and $v_{\max}$ denotes the maximum channel Doppler shift.

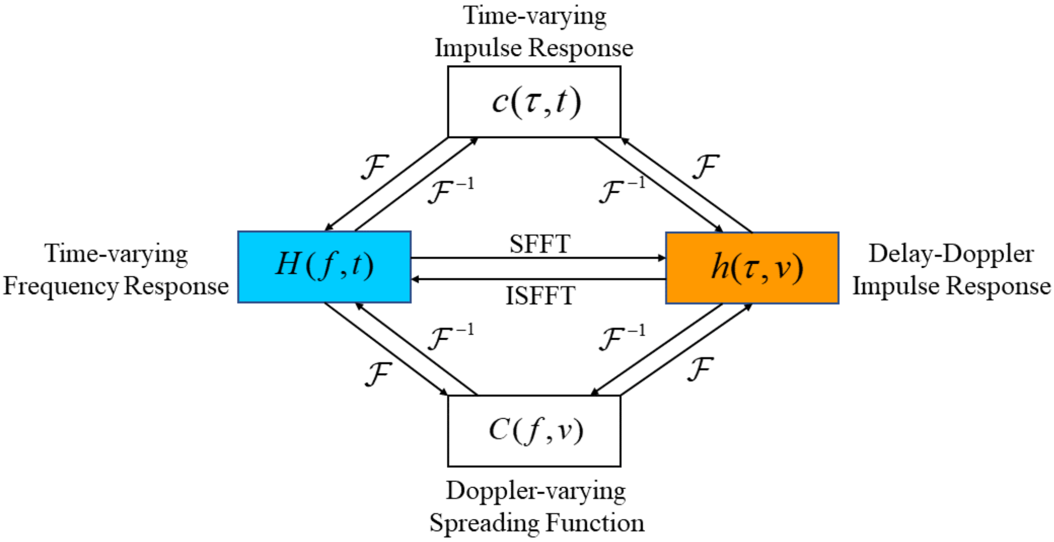

Figure 7 Different representations of the LTV channel.

2.3 Physical Discrete-Path Model

Among the different representations of the LTV channel mentioned above, the disadvantage of $c(\tau,t)$ and $H(t,f)$ is that both of them might be limited by the maximum channel delay $\tau_{\max}$ and the maximum channel Doppler shift $v_{\max}$ [52]. In this case, the changing rate of the channel coefficient is proportional to the reciprocal of coherent time, and its value will be determined by the operating frequency and the moving speed. Therefore, the channel varies very fast when it works in the high mobility and high operating frequency scenario, which makes it hard to do channel estimation and equalization[53]. However, $h(\tau,v)$ combines the communication model with the physical scenario in the delay-Doppler domain. Because the parameters delay and Doppler shift are directly related to the physical quantities distance and speed, respectively[54].

In the physical discrete-path model, the explicit channel characteristics are obtained mainly through the physical propagation paths[55]. The physical effects of the time-frequency doubly-dispersive channel are mainly multipath propagation and the Doppler effect[56]. Assume that a finite number of paths are modeled between the transmitter and the receiver. Then $h(\tau,v)$ can be modeled by

$$h(\tau,v)=\sum_{i=1}^{P}h_i\delta\left(\tau-\tau_i\right)\delta\left(v-v_i\right) \tag{2-13}$$

where P is the number of paths, τ_i and v_i are the channel delay and Doppler shift in the ith path, $\delta\left(\bullet\right)$ is the Dirac function, and $h_i=\left|h_i\right|e^{j\theta_i}$ denotes the complex path gain, in which the path phase in the ith path θ_i is uniformly distributed on $[-\pi,\pi]$ and independent of different paths.

From equation (2-12) and (2-13), the time domain input-output realation in the discrete-path model can be calculated by

$$r(t)=\sum_{i=1}^{P}h_i s(t-\tau_i)e^{j2\pi v_i t} \tag{2-14}$$

From equation (2-10) and (2-13), $H(f,t)$ can be calculated by

$$H(f,t)=\sum_{i=1}^{P}h_i e^{-j2\pi\tau_i f}e^{j2\pi v_i t} \tag{2-15}$$

Assuming the carrier frequency is 77 GHz, the maximum relative speed between the transmitter and receiver is $V_{\max} = 500\ \mathrm{km/h}$. In this case, the maximum Doppler shift is $v_{\max} = 35.65\ \mathrm{KHz}$. We set 10 propagation paths in the multipath channel[57], where the Doppler shift in each path is distributed uniformly on $[-v_{\max}, v_{\max}]$. And the complex path gain in each path obeys the Gaussian distribution with zero mean and equal variance, which can be expressed as $h_i \sim \mathcal{CN}(0,1/P)$.

The delay-Doppler impulse response $h(\tau,v)$ and the time-varying frequency response $H(f,t)$ are plotted in Figure 8 and Figure 9, respectively. $H(f,t)$ in Figure 8 shows that channel is fast time-varying in the TF domain, which may make it hard to do channel estimation. However, $h(\tau,v)$ in Figure 9 shows that the channel impulse response is much more compact and sparse in the DD domain.

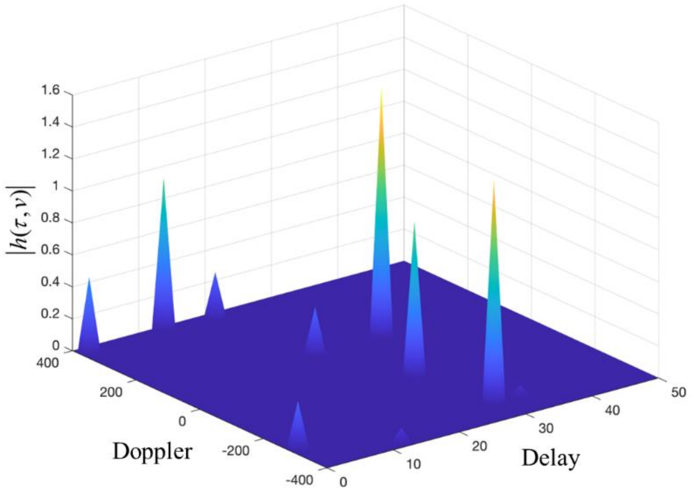

Figure 8 Delay-Doppler impulse response.

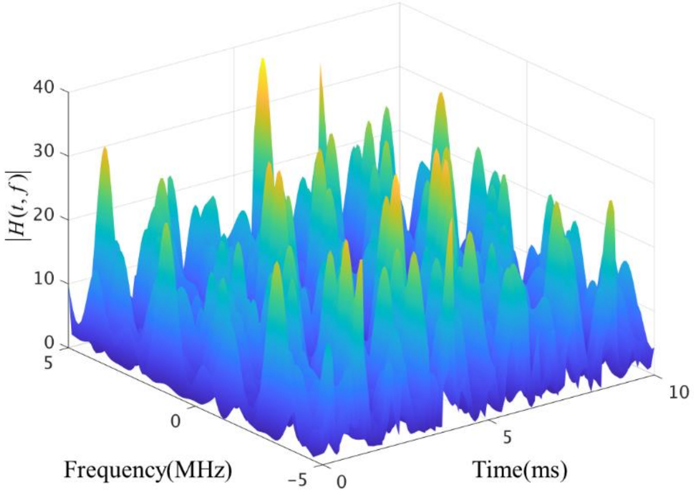

Figure 9 Time-varying frequency response.

2.4 Summary of the Chapter

In this chapter, the transmission characteristics of the wireless channel are first classified into several types of fading, which are path loss, shadow fading, frequency non-selective fading, frequency-selective fading, slow fading, and time-selective fading. Then, four equivalent representations of the LTV channel in different domains and the transformation relations from one to the other are introduced. After building the physical discrete-path model, the channel response in the TF domain and DD domain are plotted, which shows that the channel response is sparse in the DD domain but fast time-varying in the TF domain.

Chapter Three OTFS Principle and Analysis

In this chapter, the OTFS system model is first introduced from the transmitter to the receiver and compare the reduced CP and full CP in OTFS. Then, the input-output relations are derived and the interferences in different domains are analyzed. Moreover, the equivalence between time domain ZF equalization and the DD domain ZF equalization is proved, as well as the MMSE equalization.

3.1 OTFS Principle

OFDM is a traditional multi-carrier modulation technology, widely used in 4th generation (4G) and 5th generation (5G). OFDM converts high-speed serial data into low-speed parallel data by frequency multiplexing, which has good resistance to multipath fading. However, in the high-mobility scenario requested in 6G, the orthogonality of the subcarriers will be severely damaged due to the high Doppler. Thus, OTFS is introduced as a new multi-carrier modulation technology instead of OFDM to solve the high-Doppler problem in the 6G scenario. OTFS modulates information symbols onto a set of two-dimensional orthogonal basis functions in the Delay-Doppler domain, where the channel impulse response is sparse.

On the one hand, OTFS modulation can be treated as a precoding module added to the traditional OFDM modulation scheme, which makes OTFS highly compatible with OFDM and enables the OTFS technology to be implemented in practical engineering[56-58]. This way of OTFS modulation scheme based on OFDM is shown in Figure 10.

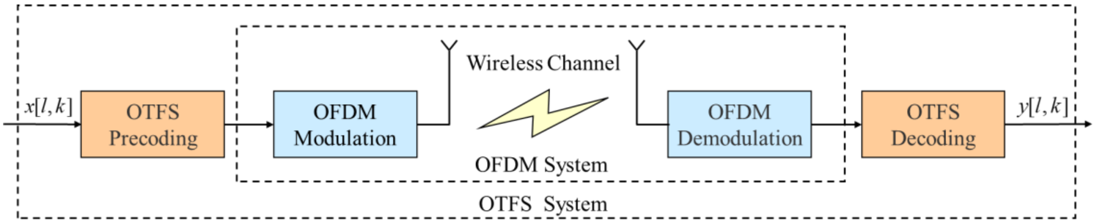

Figure 10 OTFS modulation scheme based on OFDM.

On the other hand, the OTFS system can also be realized in a more general way, as shown in Figure 11. In the following sections, we will mainly introduce the second way, which can achieve higher spectrum efficiency. The difference between Figure 10 and Figure 11 is mainly reflected in their CP insertion method, which will be declared in section 3.1.1 specifically.

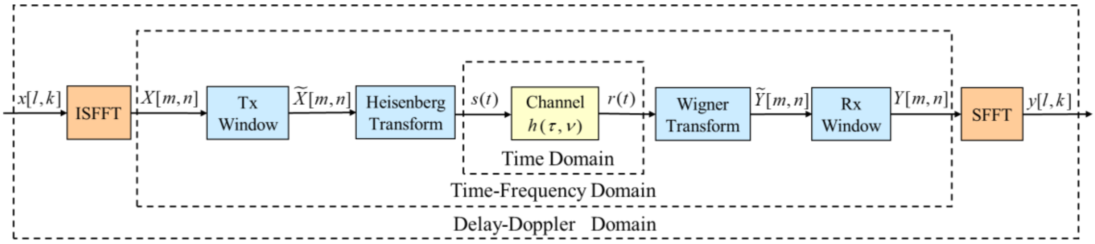

Figure 11 Generalized OTFS modulation scheme.

3.1.1 Transmitter

In this OTFS system, the source information is considered as a sequence of QAM symbols denoted as a column vector $\mathbf{d}$, whose length is $M \times N$. Then, the QAM symbols are distributed onto the two-dimensional delay-Doppler grid as one frame of OTFS symbols, which can be expressed as

$$x_{\mathrm{DD}}[k,l],\ k=0,\ldots,N-1\ and\ \ l=0,\ldots,M-1, \tag{3-1}$$

where M represents the number of subcarriers and N represents the number of the symbol points. And its corresponding matrix form is given by

$$\mathbf{X}_{DD} \in \mathbb{C}^{M\times N}. \tag{3-2}$$

The QAM symbols on the DD grid will be modulated onto the TF grid by ISFFT, which is a two-dimensional orthogonal transformation. The discrete DD grid and TF grid are shown in Figure 12. The transformation can be expressed as

$$X_{TF}\left[n,m\right]=\frac{1}{\sqrt{NM}}\sum_{k=0}^{N-1}\sum_{l=0}^{M-1}x_{DD}\left[k,l\right]e^{j2\pi\left(\frac{nk}{N}-\frac{ml}{M}\right)}, \tag{3-3}$$

where $,n=0,\cdots,N-1$ and $m=0,\cdots,M-1$. The equation (3-3) shows that ISFFT can be realized by the combination of M-point DFT and N-point IDFT. Thus, the matrix form of ISFFT is given by

$$\mathbf{X}_{TF}=\mathbf{F}_M\mathbf{X}_{DD}\mathbf{F}_N^{\mathrm{H}}, \tag{3-4}$$

where $\mathbf{F}_M=\{\frac{1}{\sqrt{M}}e^{2\pi jkl/M}\}_{k,l=0}^{M-1}$ represents the normalized M-point DFT matrix, and $(\bullet)^{\mathbf{H}}$ represents the conjugate transpose of the matrix.

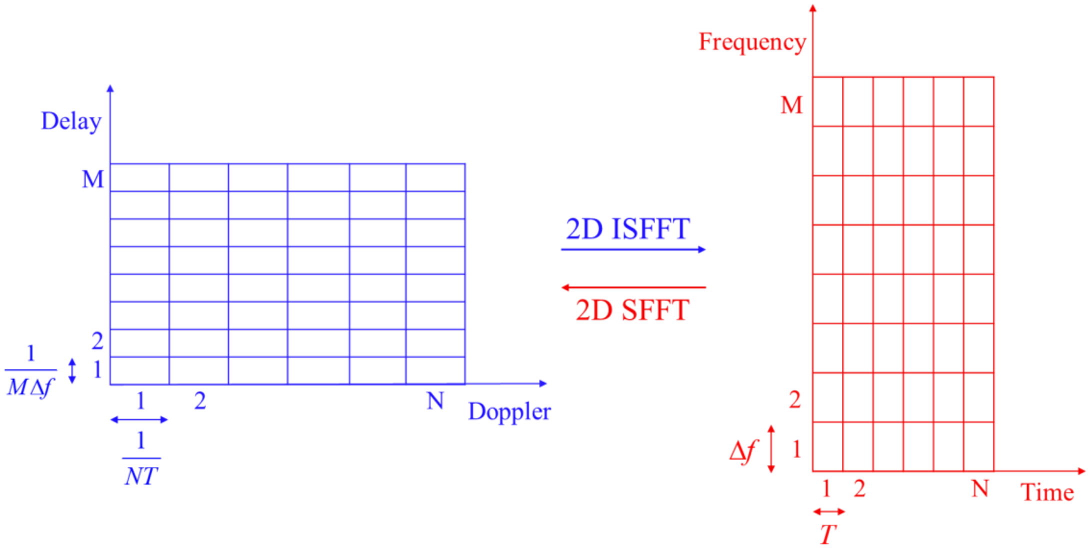

Figure 12 Discrete DD grid and TF grid.

The discrete data symbols are then multiplied by a windowing function denoted as W_{tx} in the TF domain, which can be expressed as

$$X_{TF}\left[n,m\right]=X_{TF}\left[n,m\right]W_{tx}\left[n,m\right], \tag{3-5}$$

whose corresponding matrix form is given by

$$\mathbf{X}_{TF} = \mathbf{X}_{TF} \odot \mathbf{W}_{tx}, \tag{3-6}$$

where $\odot$ is called the point-wise multiplication or Hadamard product and $\mathbf{W}_{tx}$ is the matrix form of W_{tx}.

Since the point-wise multiplication in the TF domain is equivalent to a 2D circular convolution in the DD domain, the TF domain window can be treated as a DD domain filter to improve the sparsity of the effective channel in the DD domain. Moreover, the windowing function can be designed for various purposes, such as shortening the channel response in the DD domain, mitigating the effects of ISI and ICI caused by multipath propagation and LTV channels, and making the receiver perform efficient channel equalization and demodulation by concentrating the energy of the transmitted symbols in a compact region of the time-frequency plane.

The choice of the windowing function depends on the specific requirements of the communication system and the characteristics of the channel. Some commonly used windowing functions for OTFS include rectangular, Hamming, and Kaiser-Bessel functions. The optimal windowing function can be determined by analyzing the trade-off between spectral efficiency, computational complexity, and ISI/ICI suppression.

Then, the window-filtered discrete signal in the TF domain is transformed into the continuous time domain signal by the Heisenberg transform, which can be expressed as

$$s(t) = \sum_{n=0}^{N-1} \sum_{m=0}^{M-1} X_{TF}[n, m] g_{tx}(t - nT) e^{j2\pi m\Delta f(t-nT)}, \tag{3-7}$$

where Δf is the frequency grid spacing which is also called the subcarrier spacing, T is time grid spacing which is also called the OTFS symbol duration, and $g_{tx}(t)$ is the pulse-shaping filter function at the transmitter. To guarantee the orthogonality of the multi-carrier modulation, $\mathrm{T}\Delta f = 1$ should be satisfied. The corresponding matrix form of the Heisenberg transform is given by

$$\mathbf{S}_T = \mathbf{G}_{tx}\mathbf{F}_M^H\mathbf{X}_{TF}\ , \tag{3-8}$$

$$\boldsymbol{s}_T = vec(\boldsymbol{S}_T)\ , \tag{3-9}$$

where $\mathbf{G}_{tx} = diag\left[g_{tx}(0), g_{tx}(T/M), \ldots, g_{tx}((M-1)T/M)\right]$ is the pulse-shaping filtering matrix at the transmitter, and $vec(\bullet)$ represent the column vectorization operation.

Before launching into the wireless media by RF antenna, some CP should be added to the time signal $\boldsymbol{s}_T$, and the details will be presented in the next section.

During the wireless transmission, the multipath effect will cause the time spread, as we introduced in section 2.1. Due to the existence of the time spread, the tail of the previous symbol will fall into the sampling interval of this symbol, which causes ISI. And the orthogonality of the subcarriers is also destroyed, which causes ICI.

To resist ICI and ISI caused by time spread, we introduce the definition of CP. which copies the last few bits of the symbol at the tail and pastes to the head. After adding CP, the transmitted symbols could transform the linear convolution with the channel response into cyclic convolution, through which it resists the ICI and ISI caused by the time spread. Thus, the cyclic characteristics make the receiver can get the whole symbol even with the presence of delay, as long as the delay spread is shorter than the CP duration.

However, if the total length of CP is too long, it will take a lot of spectrum efficiency.

Thus, we introduce the Reduced CP, in which only one CP is added to one OTFS frame, compared with the traditional Full CP, in which multiple CPs are added to one OTFS frame. The RCP and FCP are shown in Figure 13.

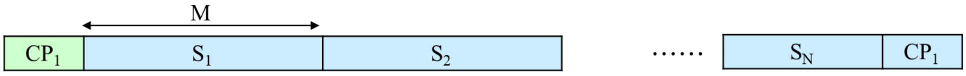

(a) Reduced Cyclic Prefix.

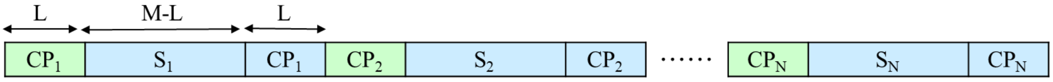

(b) Full Cyclic Prefix.

Figure 13 Different Cyclic Prefixes in OTFS systems.

The operation of adding CP to the column vector $\boldsymbol{s}_T$ can be written in the matrix

$$\boldsymbol{s}_T^{CP} = A^{CP} s_T , \tag{3-10}$$

where A^{CP} is the CP addition matrix. The length of the CP is denoted as l_{CP}, which should be larger than the channel delay spread $l_{\max}$, which can be expressed as $l_{CP} \geq l_{\max}$. To be more specific, in the RCP model, the CP addition matrix A^{CP} can be written as

$$\mathbf{A}^{CP} = \left[\mathbf{G}^{CP}, \mathbf{I}_{MN}\right]^T , \tag{3-11}$$

where $\mathbf{G}^{CP} \in \mathbb{C}^{MN \times M^{CP}}$ is formed by taking the last $l_{\max}$ columns of the identity matrix $\mathbf{I}_{MN}$.

When using the Reduced CP, the corresponding expression is given by

$$s'(t) = \begin{cases} s\left(t + NT - \dfrac{l_{CP}}{M\Delta f}\right) & , 0 < t < \dfrac{l_{CP}}{M\Delta f} \\ s\left(t - \dfrac{l_{CP}}{M\Delta f}\right) & , \dfrac{l_{CP}}{M\Delta f} < t < \dfrac{l_{CP}}{M\Delta f} + NT \end{cases} , \tag{3-12}$$

After the CP is added to the data symbols, the time domain signal is then modulated onto the carriers and emitted to the wireless channel by RF antenna, which will be discussed in more detail in the next section.

3.1.2 Channel

In this OTFS system, we will use the physical discrete-path channel model mentioned in the previous sections. As declared in section 2.1.4, the complex baseband impulse response $h(\tau,v)$ of a doubly-dispersive multipath channel can be expressed as

$$h(\tau,v)=\sum_{i=1}^{P}h_i\delta\left(\tau-\tau_i\right)\delta\left(v-v_i\right), \tag{3-13}$$

where τ is the channel delay, v is the channel Doppler shift, P is the number of the paths, h_i, τ_i, and v_i are the channel gain, channel delay, and Doppler shift in the ith path, respectively. Among them, the representations of τ_i and v_i are given by

$$\tau_i=\frac{l_{\tau_i}+\iota_{\tau_i}}{M\Delta f}, \tag{3-14}$$

$$v_i=\frac{k_{v_i}+\kappa_{v_i}}{NT}, \tag{3-15}$$

where l_{τ_i} and ι_{τ_i} represent the integer part and the fractional part of the delay taps in the ith path, $\iota_{\tau_i} > -\frac{1}{2} . k_{v_i}$ and κ_{v_i} represents the integer part and the fractional part of the Doppler taps in the ith path, $-\frac{1}{2} < \kappa_{v_i} < \frac{1}{2}$.

In the practical wireless channel paths, the delay and Doppler may not be integer multiple of $\Delta\tau=\frac{1}{M\Delta f}$ and $\Delta v=\frac{1}{NT}$, respectively. It means signal paths may not be on the DD grid points but inside, which causes the problems of fractional delay and fractional Doppler.

The delay resolution $\Delta\tau$ can be improved by increasing M the number of subcarriers when the subcarrier spacing is fixed. Since the bandwidth and the number of subcarriers M are very large in practical multi-carrier systems, the sampled path delays can be approximated as integers, and the fractional parts of the delay taps can be ignored.

However, if the Doppler resolution is improved by increasing N the symbol points, which also increases the symbol duration NT. In this way, if the symbol duration $T_s = NT$ is increased to be larger than coherent time T_c, the signal will go through a time-selective fading as mentioned in section 2.1.4. So the impact of fractional parts of Doppler taps κ_{ν_i} cannot be easily ignored.

A concise representation of the channel response is given by

$$\mathbf{H}_T = \sum_{P}^{i=1} h_i \mathbf{\Pi}^{l_{\tau_i}} \Delta^{k_{\nu_i}}, \tag{3-16}$$

where $\mathbf{\Pi}^{l_{\tau_i}}$ represents the impact of the channel delay in the ith path, which means the signal in this path reaches the receiver by left circular shifting l_{τ_i} symbols. And $\Delta^{k_{\nu_i}}$ is a diagonal matrix representing the impact of the channel Doppler shift, which makes the phrase increase with symbol coordinates increasing. The details of $\mathbf{\Pi}^{l_{\tau_i}}$ and $\Delta^{k_{\nu_i}}$ are given by

$$\mathbf{\Pi}^{l_{\tau_i}} = \text{circshift}\left(\mathbf{I}_{MN\times MN}, l_{\tau_i}\right) = \begin{bmatrix} 0 & \cdots & 0 & 1 \\ 1 & \ddots & 0 & 0 \\ \vdots & \ddots & \ddots & \vdots \\ 0 & \cdots & 1 & 0 \end{bmatrix}_{MN\times MN}, \tag{3-17}$$

$$\begin{aligned} \Delta^{k_{\nu_i}} &= \text{diag}\left\{e^{j2\pi\nu_i n T_s}\right\}, \quad n = 0,1,\ldots,MN-1 \ \ and \ \ T_s = T/M \\ &= \text{diag}\left[1, e^{\frac{j2\pi\times1}{MN}}, e^{\frac{j2\pi\times2}{MN}}, e^{\frac{j2\pi\times3}{MN}}, \ldots, e^{\frac{j2\pi(MN-1)}{MN}}\right] \end{aligned}. \tag{3-18}$$

Notice that though the channel matrix $\mathbf{H}_T$ is the matrix form of the delay-Doppler response, it can also be considered as the effective channel in the time domain before adding CP and after discarding CP.

3.1.3 Receiver

At the receiver, the expression of the attached signal with CP is given by

$$r'(t)=\iint h(\tau,v)s'(t-\tau)e^{j2\pi v(t-\tau)}d\tau dv+w'(t)\text{ ,} \tag{3-19}$$

where $w'(t)$ is the time domain additive white Gaussian noise (AWGN) with the presence of CP. Substitute equation (3-13) into equation (3-19), we can get

$$r'(t)=\sum_{i=1}^{p}h_i e^{j2\pi v_i(t-\tau_i)}s'\left(t-\tau_i\right)+w'(t)\text{ ,} \tag{3-20}$$

To simplify the derivation, here we consider no fractional delay and fractional Doppler, which means $\iota_i=0$ and $\kappa_i=0$. In this case, we substitute equation (3-14) and (3-15) into equation (3-20), then we can get

$$r'(t)=\sum_{i=1}^{p}h_i e^{j2\pi\frac{k_i}{NT}\left(t-\frac{l_i}{M\Delta f}\right)}s'\left(t-\frac{l_i}{M\Delta f}\right)+w'(t)\cdot \tag{3-21}$$

Next, we sample the received signal $r'(t)$ to the discrete one with the sampling period $T_s=\frac{NT}{MN}=\frac{T}{M}$, which can be expressed as

$$r'\left(n\right)=\sum_{i=1}^{p}h_i e^{j2\pi\frac{k_i(n-l_i)}{NM}}s'\left(n-l_i\right)+w'(n)\text{ ,} \tag{3-22}$$

where $w'(n)$ represents the AWGN in the discrete-time domain. Then, the CP in the discrete-time domain signal $r'\left(n\right)$ will be removed. The expression of the received signal in the discrete-time domain before adding CP and after discarding CP is given by

$$r\left(n\right)=\sum_{i=1}^{p}h_i e^{j2\pi\frac{k_i(n-l_i)}{MN}}s\left([n-l_i]_{MN}\right)+w(n)\text{ ,} \tag{3-23}$$

where $r\left(n\right)$ and $w(n)$ are the discrete time domain representations after discarding CP, and $[\bullet]$ denotes the modular operation[58]. The corresponding representations of the equation (3-23) in the simplified matrix form are given by

$$\mathbf{r}_T = \mathbf{H}_T\mathbf{s}_T + \mathbf{w}_T, \tag{3-24}$$

$$\mathbf{R}_T = \mathbf{vec}^{-1}(\mathbf{r}_T), \tag{3-25}$$

where the time domain effective matrix $\mathbf{H}_T$ has been declared in equation (3-16), and $\mathbf{vec}^{-1}(\bullet)$ is the inverse of the $\mathbf{vec}(\bullet)$ operation. The vector $\mathbf{w}_T$ denotes AWGN noise in the discrete-time domain, and its distribution is given by

$$\mathbf{w}_T \sim \mathcal{CN}(0,\sigma^2), \tag{3-26}$$

where $\mathbf{I_{MN}}$ denotes an MN-dimensional identity matrix, and σ^2 denotes the variance.

We denote $r(t)$ as the CP discarded version of $r'(t)$. Then the cross-ambiguity function of the receiving matched filter $A_{g_{\mathrm{rx}},r}(t,f)$ is given by

$$Y(t,f) = A_{g_{\mathrm{rx}},r}(t,f) \triangleq \int_{t'} g^*_{\mathrm{rx}}(t'-t)r(t')e^{-j2\pi f(t'-t)}dt', \tag{3-27}$$

where $g_{rx}(t)$ is the pulse-shaping filter at the receiver and $(\bullet)^*$ denotes the complex conjugation[59].

Then in the TF domain, the continuous signal is sampled to be a discrete signal, which can be expressed as

$$Y_{TF}[n,m] = Y[t,f]\Big|_{t=nT,f=m\Delta f}, \text{for } m=0,\cdots,M-1 \text{ and } n=0,\cdots,N-1. \tag{3-28}$$

The cross-ambiguity function (3-27) and the sampling function (3-28) are merged to be the Wigner transform, which transforms a continuous time domain signal into a discrete signal. Thus, the overall expression of the Wigner transform can be expressed as

$$Y_{TF}[n,m] = \int_{t'} g^*_{\mathrm{rx}}(t'-nT)r(t')e^{-j2\pi m\Delta f(t'-nT)}dt', \tag{3-29}$$

whose corresponding matrix form of Wigner Transform is given by

$$\mathbf{Y}_{TF} = \mathbf{F}_M \mathbf{G}_{rx} \mathbf{R}_T , \tag{3-30}$$

where $\mathbf{G}_{rx} = diag\left[g_{rx}(0), g_{rx}(T/M), \cdots, g_{rx}((M-1)T/M)\right]$.

The data after the are Wigner transform then multiplied by a TF domain windowing function denoted as W_{rx} at the receiver, which can be expressed as

$$Y_{TF}\left[n,m\right] = Y_{TF}\left[n,m\right] W_{rx}\left[n,m\right], \tag{3-31}$$

whose corresponding matrix form is given by

$$\mathbf{Y}_{TF} = \mathbf{Y}_{TF} \odot \mathbf{W}_{rx} , \tag{3-32}$$

where $\mathbf{W}_{rx}$ is the matrix form of W_{rx}.

Then, we transform the windowed data in the TF domain into the DD domain by SFFT, which can be expressed as

$$y_{DD}[k,l] = \frac{1}{\sqrt{NM}} \sum_{n=0}^{N-1} \sum_{m=0}^{M-1} Y_{TF}[n,m]\, e^{-j2\pi\left(\frac{nk}{N} - \frac{ml}{M}\right)}, \tag{3-33}$$

3.2 Time-Frequency Domain Analysis

In the following sections of this chapter, we will derive the input-output relation under different conditions. To simplify the derivation, we consider no CP and set all the values of the windowing functions to unity.

3.2.1 Input-Output Relation in TF Domain for Arbitrary Waveform

We first derive the input-output relation in the TF domain for the arbitrary in the expression form, which starts from substituting the (3-19) into (3-27)

$$Y(t,f) = \int_{t'} g_{\mathrm{rx}}^{*}\left(t'-t\right)\left[\int_{v}\int_{\tau} h\left(\tau,v\right) s\left(t'-\tau\right) e^{j2\pi v\left(t'-\tau\right)} d\tau dv + w\left(t'\right)\right] e^{-j2\pi f\left(t'-t\right)} dt' . \tag{3-34}$$

Then, by substituting (3-7) into (3-34), we obtain

$$Y(t,f) = \sum_{n'=0}^{N-1} \sum_{m'=0}^{M-1} X_{TF}[n',m'] \left\{ \int_{v}\int_{\tau} h\left(\tau,v\right) \left[\int_{t'} g_{\mathrm{rx}}^{*}\left(t'-t\right) g_{tx}\left(t'-\tau-n'T\right) e^{j2\pi m'\Delta f\left(t'-\tau-n'T\right)} \right.\right.$$

$$e^{j2\pi v(t'-\tau)}\, e^{-j2\pi f(t'-t)}dt'\Big]d\tau dv\Big\} + \int_{t'} g_{\mathrm{rx}}^{*}\left(t'-t\right)w\left(t'\right)e^{-j2\pi f(t'-t)}dt' . \tag{3-35}$$

After sampling $Y(t, f)$ with $t = nT$ and $f = m\Delta f$, we get its discrete version, which is shown as equation (3-36)

$$\begin{aligned} Y_{TF}\left[n,m\right] = \sum_{n'=0}^{N-1}\sum_{m'=0}^{M-1} X_{TF}[n',m']\Big\{\int_{v}\int_{\tau} h\left(\tau,v\right)\Big[\int_{t'} g_{\mathrm{rx}}^{*}\left(t'-nT\right)g_{tx}\left(t'-\tau-n'T\right)e^{j2\pi m'\Delta f(t'-\tau-n'T)} \\ e^{j2\pi v(t'-\tau)}\, e^{-j2\pi m\Delta f(t'-nT)}dt'\Big]d\tau dv\Big\} + \int_{t'} g_{\mathrm{rx}}^{*}\left(t'-nT\right)w\left(t'\right)e^{-j2\pi m\Delta f(t'-nT)}dt' , \end{aligned} \tag{3-36}$$

where the last term $\int_{t'} g_{\mathrm{rx}}^{*}\left(t'-nT\right)w\left(t'\right)e^{-j2\pi m\Delta f(t'-nT)}dt'$ satisfies the definition declared in equation (3-27). Thus, the last term can be rewritten as a cross-ambiguity function $A_{g_{\mathrm{rx}},w}\left[nT, m\Delta f\right]$ and defined as $W_{TF}\left[n,m\right]$. Then, the input-output relation for the arbitrary waveform is given by

$$Y_{TF}\left[n,m\right] = \sum_{n'=0}^{N-1}\sum_{m'=0}^{M-1} X_{TF}[n',m']H_{n,m}[n',m'] + W_{TF}\left[n,m\right], \tag{3-37}$$

where

$$\begin{aligned} H_{n,m}[n',m'] = \int_{v}\int_{\tau} h\left(\tau,v\right)\Big[\int_{t'} g_{\mathrm{rx}}^{*}\left(t'-nT\right)g_{tx}\left(t'-\tau-n'T\right) \\ \times\ e^{j2\pi m'\Delta f(t'-\tau-n'T)}e^{j2\pi v(t'-\tau)}e^{-j2\pi m\Delta f(t'-nT)}dt'\Big]d\tau dv . \end{aligned} \tag{3-38}$$

By substituting $t'' = t' - \tau - n'T$ and $t' = t'' + \tau + n'T$ into equation (3-38), we get

$$\begin{aligned} H_{n,m}[n',m'] = \int_{v}\int_{\tau} h\left(\tau,v\right)\Big[\int_{t''} g_{\mathrm{rx}}^{*}\left(t''-\left(n-n'\right)T+\tau\right)g_{tx}(t'') \\ \times\ e^{j2\pi m'\Delta f t''}e^{j2\pi v(t''+n'T)}e^{-j2\pi m\Delta f\left[t''-(n-n')T+\tau\right]}dt''\Big]d\tau dv . \end{aligned} \tag{3-39}$$

We rearrange the exponential part of the equation (3-39) to get

$$\begin{aligned} H_{n,m}[n',m'] = \int_{v}\int_{\tau} h\left(\tau,v\right)\Big[\int_{t''} g_{rx}^{*}(t''-(n-n')T+\tau)g_{tx}(t'')e^{-j2\pi\left[(m-m')\Delta f-v\right]\left[t''-(n-n')T+\tau\right]}dt''\Big] \\ \times e^{j2\pi(v+m'\Delta f)\left[(n-n')T-\tau\right]}e^{j2\pi vn'T}d\tau dv \cdot \end{aligned} \tag{3-40}$$

We can observe that $\int_{t''} g_{rx}^{*}(t''-(n-n')T+\tau)g_{tx}(t'')e^{-j2\pi\left[(m-m')\Delta f-v\right]\left[t''-(n-n')T+\tau\right]}dt''$ also satisfies the cross-ambiguity function due to equation (3-27). Thus, equation (3-40) can be rewritten as

$$H_{n,m}[n',m'] = \int_{\nu}\int_{\tau} h(\tau,\nu) A_{g_{\mathrm{rx}},g_{\mathrm{tx}}}\left[(n-n')T-\tau,(m-m')\Delta f-\nu\right]$$
$$\times e^{j2\pi(\nu+m'\Delta f)[(n-n')T-\tau]} e^{j2\pi\nu n'T} d\tau d\nu \cdot \quad (3\text{-}41)$$

Moreover, the following matrix form of the input-output relation in the TF domain corresponding to the equation (3-37) is given by

$$\mathbf{y}_{TF} = \mathbf{H}_{TF}\mathbf{x}_{TF} + \mathbf{w}_{TF}, \quad (3\text{-}42)$$

where $\mathbf{x}_{TF}$ and $\mathbf{y}_{TF}$ correspondingly refer to the vectorized version of $\mathbf{X}_{TF}$ and $\mathbf{Y}_{TF}$. The noise vector $\mathbf{w}_{TF}$ and effective channel matrix $\mathbf{H}_{TF}$ in the TF domain are given by

$$\mathbf{w}_{TF} = (\mathbf{I}_N \otimes \mathbf{F}_M\mathbf{G}_{rx})\mathbf{w}_T, \quad (3\text{-}43)$$

$$\mathbf{H}_{TF} = (\mathbf{I}_N \otimes \mathbf{F}_M\mathbf{G}_{rx})\mathbf{H}_T(\mathbf{I}_N \otimes \mathbf{G}_{tx}\mathbf{F}_M^H), \quad (3\text{-}44)$$

where $\otimes$ denotes the Kronecker product. The relevant proof from equation (3-42) to equation (3-44) is given in Appendix A.

3.2.2 Input-Output Relation in TF Domain for Ideal Pulses

The $g_{\mathrm{tx}}(t)$ and $g_{\mathrm{rx}}(t)$ pulses are said to be ideal if they satisfy the bi-orthogonal property[10]

$$A_{g_{\mathrm{rx}},g_{\mathrm{tx}}}(t,f)\Big|_{t=nT+(-\tau_{\max},\tau_{\max}),\, f=m\Delta f+(-\nu_{\max},\nu_{\max})} = \delta[n]\delta[m]q_{\tau_{\max}}(t)q_{\nu_{\max}}(f), \quad (3\text{-}45)$$

where $q_a(x)=1$ for $x\in(-a,a)$ and zero for otherwise. Equivalently, the value of the cross-ambiguity function $A_{g_{\mathrm{rx}},g_{\mathrm{tx}}}(t,f)$ can be declared as follows

$$A_{g_{\mathrm{rx}},g_{\mathrm{tx}}}(t,f)\Big|_{t=nT+(-\tau_{\max},\tau_{\max}),\, f=m\Delta f+(-\nu_{\max},\nu_{\max})}$$
$$= \begin{cases} 1, & t\in(-\tau_{\max},\tau_{\max}) \text{ and } f\in(-\nu_{\max},\nu_{\max}) \ and\ m=n=0 \\ 0, & t\in(nT-\tau_{\max},nT+\tau_{\max}) \text{ and } f\in(m\Delta f-\nu_{\max},m\Delta f+\nu_{\max}) \ \forall mn\neq 0 \end{cases}. \quad (3\text{-}46)$$

Unfortunately, ideal pulses cannot be realized practically but can be approximated by waveforms with support concentrated as much as possible in time and frequency, given the constraints imposed by the uncertainty principle[20]. Nevertheless, it is important to study the error performance of OTFS with ideal waveforms since it serves as a lower bound on the performance of OTFS with practically realizable waveforms, such as rectangular waveforms, etc.

For the ideal pulses satisfying the bi-orthogonal property, the value of $H_{n,m}[n',m']$ is non-zero only at $n'=n$ and $m'=m$ according to equation (3-41). Hence, the following input-output relation in the TF domain for the ideal pusles can be obtained by only considering only the term with $n'=n$ and $m'=m$ of the $H_{n,m}[n',m']$, which can be expressed as

$$Y_{TF}[n,m]=H_{n,m}[n,m]X_{TF}[n,m]+W_{TF}\left[n,m\right], \tag{3-47}$$

where

$$H_{n,m}[n,m]=H_{n,m}[n',m']\big|_{n'=n,m'=m}\int_{\nu}\int_{\tau}h(\tau,\nu)e^{j2\pi\nu nT}e^{-j2\pi(\nu+m\Delta f)\tau}d\tau d\nu\ . \tag{3-48}$$

By substituting equation (3-13) into equation (3-48), we obtain

$$H_{n,m}[n,m]=\sum_{i=1}^{P}h_i\delta\left(\tau-\tau_i\right)\delta\left(\nu-\nu_i\right)e^{j2\pi\nu_i nT}e^{-j2\pi(\nu_i+m\Delta f)\tau_i}\ . \tag{3-49}$$

Then, by substituting $\tau_i=\frac{l_{\tau_i}+\iota_{\tau_i}}{M\Delta f}$ and $\nu_i=\frac{k_{\nu_i}+\kappa_{\nu_i}}{NT}$ into equation (3-49), we obtain the closed form expression of $H_{n,m}[n,m]$

$$H_{n,m}[n,m]=\sum_{i=1}^{P}h_i e^{-j2\pi\frac{\left(k_{\nu_i}+\kappa_{\nu_i}\right)\left(l_{\tau_i}+\iota_{\tau_i}\right)}{NM}}e^{j2\pi\left(\frac{n\left(k_{\nu_i}+\kappa_{\nu_i}\right)}{N}-\frac{m\left(l_{\tau_i}+\iota_{\tau_i}\right)}{M}\right)}\ . \tag{3-50}$$

However, the number of subcarriers in the practical multi-carrier system is usually large enough to increase the delay resolution to a high precision, so that the fractional part of delay taps can be ignored. Therefore, the simplified version of $H_{n,m}[n,m]$ is obtained by substituting $l_{\tau_i}=0$ into equation (3-50)

$$H_{n,m}[n,m]=\sum_{i=1}^{P}h_i e^{-j2\pi\frac{\left(k_{v_i}+\kappa_{v_i}\right)l_{\tau_i}}{NM}}e^{j2\pi\left(\frac{n\left(k_{v_i}+\kappa_{v_i}\right)}{N}-\frac{ml_{\tau_i}}{M}\right)}. \tag{3-51}$$

3.2.3 Input-Output Relation in TF Domain for Rectangular Pulses

For rectangular pulses, $A_{g_{\mathrm{rx}},g_{\mathrm{tx}}}\left[(n-n')T-\tau,(m-m')\Delta f-v\right]$ is non-zero for $|\tau|<\tau_{\max}$ and $|v|<v_{\max}$ only when $n'=n$ and $n'=n-1$, since $\mathrm{g}_{tx}(t)$ and $\mathrm{g}_{rx}(t)$ are pulses of duration T and $\tau_{\max}\ll T$. In this condition, the expression form of the input-output relation in the TF domain is given by

$$\begin{aligned}Y_{TF}[n,m]=&\sum_{n'=n-1}^{n}\sum_{m'=0}^{M-1}H_{n,m}[n',m']X_{TF}[n',m']+W_{TF}[n,m]=H_{n,m}[n,m]X_{TF}[n,m]\\&+\sum_{m'=0,m'\neq m}^{M-1}H_{n,m}[n,m']X_{TF}[n,m']+\sum_{m'=0}^{M-1}H_{n,m}[n-1,m']X_{TF}[n-1,m']+W_{TF}[n,m].\end{aligned} \tag{3-52}$$

The rectangular pulse is non-zero only in $[0,T]$. The convolution of two rectangular signals is a triangle. Similarly, a cross-ambiguity function is equivalent to a 2D correlator, and the modulus of the output is also a triangle which is non-zero only in $[-T,T]$. According to $A_{g_{\mathrm{rx}},g_{\mathrm{tx}}}\left[(n-n')T-\tau,(m-m')\Delta f-v\right]$, only when $n'=n$ and $n'=n-1$, the time t is in $[-T,T]$, and only in this condition the cross-ambiguity function is non-zero.

$Y_{TF}[n,m]$ in the arbitrary waveform has $M\times N$ terms. The number is reduced to $2M$ terms in rectangular pulses. The first term shows the condition when $n'=n$ and $m'=m$. The second term shows the condition when $n'=n$ and $m'\neq m$, which is called ICI. The third term shows the condition when $n'=n-1$, which is called ISI.

When using the rectangular waveform, the Wigner transform is then reduced to the traditional DFT. Therefore, by substituting $\mathbf{G}_{rx}=\mathbf{I}_M$ into equation (3-43) and equation (3-44), the effective channel matrix and noise vector in the TF domain for rectangular pulses are given by

$$\mathbf{w}_{TF} = (\mathbf{I}_N \otimes \mathbf{F}_M)\mathbf{w}_T, \tag{3-53}$$

$$\mathbf{H}_{TF} = (\mathbf{I}_N \otimes \mathbf{F}_M)\mathbf{H}_T(\mathbf{I}_N \otimes \mathbf{F}_M^H). \tag{3-54}$$

We observe that $\mathbf{I}_N \otimes \mathbf{F}_M$ is an orthogonal matrix, so that the TF domain noise vector $\mathbf{w}_{TF}$ follows the same statistical distribution as the time domain noise vector $\mathbf{w}_T$. Moreover, the energy of the time domain noise vector remains unchanged after left-multiplying the unitary matrix $\mathbf{I}_N \otimes \mathbf{F}_M$.

3.2.3.1 ICI Analysis in TF Domain for Rectangular Pulses

Fixed n and m note that the cross ambiguity function in the $H_{n,m}[n,m'], m' \neq m$ term of ICI, $A_{g_{\mathrm{rx}},g_{\mathrm{tx}}}\left[-\tau,(m-m')\Delta f - \nu\right]$, is independent of n, and is computed for the $i-th$ channel path with delay τ_i and Doppler ν_i as

$$A^{ICI} \triangleq \int g_{\mathrm{rx}}^*(t'+\tau_i)g_{\mathrm{tx}}(t')e^{-j2\pi((m-m')\Delta f-\nu_i))(t'+\tau_i)}dt'. \tag{3-55}$$

Discard the dependency of A^{ICI} on (m,m',τ_i,ν_i) for simplicity. Since the received signal is sampled of $1/M$ (or $1/M\Delta f$), A^{ICI} can be computed as

$$A^{ICI} = \frac{1}{M}\sum_{p=0}^{M-1-l_{\tau_i}} e^{-j2\pi((m-m')\Delta f-\nu_i))\left(\frac{p}{M\Delta f}+\tau_i\right)}. \tag{3-56}$$

Recall that the pulses $g_{\mathrm{tx}}(t)$ and $g_{\mathrm{rx}}(t)$ have duration T, and l_{τ_i} is the delay tap. The amplitude A^{ICI} is

$$\left|A^{ICI}\right| = \left|\frac{1}{M}\sum_{p=0}^{M-1-l_{\tau_i}} e^{-j2\pi((m-m')\Delta f-\nu_i))\left(\frac{p}{M\Delta f}+\tau_i\right)}\right| \tag{3-57}$$

$$= \frac{\left|e^{-j2\pi\left(m-m'-\frac{k_{\nu_i}+\kappa_{\nu_i}}{N}\right)\frac{M-l_{\tau_i}}{M}}-1\right|}{\left|Me^{-j2\pi\left(m-m'-\frac{k_{\nu_i}+\kappa_{\nu_i}}{N}\right)\frac{1}{M}}-M\right|}. \tag{3-58}$$

Obviously, the value of $\left|A^{ICI}\right|$ decreases as m' moves away from m. It implies that ICI becomes less as the interfering subcarriers are further away from the interfered subcarrier. Also, larger the Doppler causes larger the number of neighboring subcarriers that interfere with the present subcarrier, which is similar to the fractional Doppler effect.

3.2.3.2 ISI Analysis in TF Domain for Rectangular Pulses

Similar to the ICI analysis, the cross-ambiguity function in the $H_{n,m}[n-1,m']$ term of ISI, $A^{ISI}=A_{g_{\mathrm{rx}},g_{\mathrm{tx}}}\left[T-\tau,\left(m-m'\right)\Delta f-v\right]$, is computed for the $i-th$ channel path as

$$A^{ISI}=\frac{1}{M}\sum_{p=M-l_{\tau_i}}^{M-1}e^{-j2\pi((m-m')\Delta f-v_i)\left(\frac{p}{M\Delta f}+\tau_i-T\right)}. \tag{3-59}$$

The amplitude $\left|A^{ISI}\right|$ also has similar properties of $\left|A^{ICI}\right|$, where it reduces as m' moves away from m implying that the ISI is smaller for the interfering symbols further away (in the frequency axis) from the interfered symbol.

Note that the terms that effect the ICI and ISI are mutually exclusive, i.e., $p=0$ to $M-1-l_{\tau_i}$ contributes to ICI whereas $p=M-l_{\tau_i}$ to $M-1$ contributes to ISI. This property helps in differentiating the ICI and ISI effects in the delay-Doppler domain.

3.3 Delay-Doppler Domain Analysis

In section 3.3, we will derive the input-output relation and analyze the IDI in the DD domain. Moreover, we will give the representation of the effective channel matrix in the DD domain, to provide the theoretical basis for the following research on equalization in section 3.4.

3.3.1 Input-Output Relation in DD Domain for Arbitrary Waveform

The matrix form of the input-output relation in the DD domain for arbitrary waveform is given as follows

$$\mathbf{y}_{DD}=\mathbf{H}_{DD}\mathbf{x}_{DD}+\mathbf{w}_{DD}, \tag{3-60}$$

where $\mathbf{x}_{DD}$ and $\mathbf{y}_{DD}$ correspondingly refer to the vectorized version of $\mathbf{X}_{DD}$ and $\mathbf{Y}_{DD}$. The noise vector $\mathbf{w}_{DD}$ and effective channel matrix $\mathbf{H}_{DD}$ in the DD domain are given by

$$\mathbf{w}_{DD}=(\mathbf{F}_N\otimes\mathbf{G}_{rx})\mathbf{w}_T, \tag{3-61}$$

$$\mathbf{H}_{DD}=(\mathbf{F}_N\otimes\mathbf{G}_{rx})\mathbf{H}_T(\mathbf{F}_N^H\otimes\mathbf{G}_{tx})\mathbf{x}_{DD}\cdot \tag{3-62}$$

The relevant proof is given in Appendix B.

3.3.2 Input-Output Relation in DD Domain for Ideal Pulses

In section 3.2.2, the input-output relation in the TF domain has been derived in equation (3-47). Then, the DD domain output can be obtained by doing SFFT (3-33) to the TF domain output $Y_{TF}[n,m]$

$$\mathrm{y}_{DD}[k,l]=\frac{1}{\sqrt{NM}}\sum_{n=0}^{N-1}\sum_{m=0}^{M-1}\left(H_{n,m}[n,m]X_{TF}[n,m]+W_{TF}\left[n,m\right]\right)\, e^{-j2\pi\left(\frac{nk}{N}-\frac{ml}{M}\right)}. \tag{3-63}$$

Similarly, by doing ISFFT (3-3) to the TF domain input $X_{TF}[n,m]$, we get

$$\mathrm{y}_{DD}[k,l]=\frac{1}{\sqrt{NM}}\sum_{n=0}^{N-1}\sum_{m=0}^{M-1}\left\{H_{n,m}[n,m]\left[\frac{1}{\sqrt{NM}}\sum_{k'=0}^{N-1}\sum_{l'=0}^{M-1}x_{DD}[k',l']e^{j2\pi\left(\frac{nk'}{N}-\frac{ml'}{M}\right)}\right]+W_{TF}\left[n,m\right]\right\}$$

$$\times\, e^{-j2\pi\left(\frac{nk}{N}-\frac{ml}{M}\right)}. \tag{3-64}$$

By reorganizing the terms, the equation (3-64) can be rewritten as

$$\mathrm{y}_{DD}[k,l]=\frac{1}{NM}\sum_{k'=0}^{N-1}\sum_{l'=0}^{M-1}x_{DD}[k',l']\left[\sum_{n=0}^{N-1}\sum_{m=0}^{M-1}H_{n,m}[n,m]\,e^{-j2\pi\left(\frac{k-k'}{NT}\right)nT}\;e^{j2\pi\left(\frac{l-l'}{M\Delta f}\right)m\Delta f}\right]$$

$$+\frac{1}{\sqrt{NM}}\sum_{n=0}^{N-1}\sum_{m=0}^{M-1}W_{TF}\left[n,m\right]e^{-j2\pi\left(\frac{nk}{N}-\frac{ml}{M}\right)}, \tag{3-65}$$

from which we observe that the second term satisfies the definition of SFFT (3-33), so we define $w_{DD}[k,l]=\frac{1}{\sqrt{NM}}\sum_{n=0}^{N-1}\sum_{m=0}^{M-1}W_{TF}\left[n,m\right]e^{-j2\pi\left(\frac{nk}{N}-\frac{ml}{M}\right)}$. For the first term in equation (3-65), we define

$$h_w\left[k-k',l-l'\right]=\sum_{n=0}^{N-1}\sum_{m=0}^{M-1}H_{n,m}[n,m]\,e^{-j2\pi\left(\frac{k-k'}{NT}\right)nT}\;e^{j2\pi\left(\frac{l-l'}{M\Delta f}\right)m\Delta f}. \tag{3-66}$$

where $h_w[\cdot,\cdot]$ is the sampled version of the following impulse response function

$$h_w\left[k-k',l-l'\right]=h_w(\nu,\tau)\big|_{\nu=\frac{k-k'}{NT},\tau=\frac{l-l'}{M\Delta f}}, \tag{3-67}$$

where $h_w(\nu,\tau)$ is the result of the circular convolution of the channel response $h(\tau,\nu)$ with $\omega(\tau,\nu)$

$$h_w(\nu,\tau)=\int_{\nu'}\int_{\tau'}h\left(\tau',\nu'\right)\omega\left(\nu-\nu',\tau-\tau'\right)e^{-j2\pi\nu\tau}\mathrm{d}\tau'\mathrm{d}\nu', \tag{3-68}$$

where $\omega(\nu,\tau)$ is the SFFT result of a rectangular window in the TF domain

$$\omega(\nu,\tau)=\sum_{m=0}^{M-1}\sum_{n=0}^{N-1}1\cdot e^{-j2\pi(\nu nT-\tau m\Delta f)}. \tag{3-69}$$

Therefore, the expression form of the input-output relation in the DD domain is obtained

$$y_{DD}[k,l]=\frac{1}{NM}\sum_{k'=0}^{N-1}\sum_{l'=0}^{M-1}x_{DD}[k',l']h_w\left[k-k',l-l'\right]+w_{DD}[k,l]. \tag{3-70}$$

3.3.2.1 IDI Analysis in DD Domain for Ideal Pulses

From equation (3-70) in section 3.3.2, we observe that the DD domain received signal $y_{DD}[k,l]$ is a linear combination of all the transmitted signals $x_{DD}[k',l']$, $k'=0,\ldots,N-1$, $l'=0,\ldots,M-1$. Therefore, the DD domain input-output relation for ideal pulses (3-67) can be represented as a linear system with MN variables $x_{DD}[k',l']$.

In the following, By using the sparse representation of the delay-Doppler channel (3-13), the DD domain input-output relation (3-70) can be reduced to a sparse linear system, where each received signal can be approximated as a linear combination of only a few transmitted signals.

By substituting (3-13) into (3-68), we obtain

$$h_w(\nu,\tau)=\sum_{i=1}^{P}h_i e^{-j2\pi\nu_i\tau_i}\omega(\nu-\nu_i,\tau-\tau_i)\,. \tag{3-71}$$

By substituting (3-69) into (3-71), we get

$$h_w(\nu,\tau)=\sum_{i=1}^{P}h_i e^{-j2\pi\nu_i\tau_i}\left(\sum_{n=0}^{N-1}\sum_{m=0}^{M-1}e^{-j2\pi(\nu-\nu')nT}e^{j2\pi(\tau-\tau')m\Delta f}\right) \tag{3-72}$$

$$=\sum_{i=1}^{P}h_i e^{-j2\pi\nu_i\tau_i}\mathcal{G}^{IDI}(\nu,\nu_i)\mathcal{F}^{IDI}(\tau,\tau_i)\,, \tag{3-73}$$

where we define

$$\mathcal{G}^{IDI}(\nu,\nu_i)\triangleq\sum_{n'=0}^{N-1}e^{-j2\pi(\nu-\nu_i)n'T}\,, \tag{3-74}$$

$$\mathcal{F}^{IDI}(\tau,\tau_i)\triangleq\sum_{m'=0}^{M-1}e^{j2\pi(\tau-\tau_i)m'\Delta f}\,. \tag{3-75}$$

We first evaluate $\mathcal{F}^{IDI}(\tau,\tau_i)$ at $\tau=\dfrac{l-l'}{M\Delta f}$ ass

$$\mathcal{F}^{IDI}\left(\frac{l-l'}{M\Delta f},\tau_i\right)=\sum_{m'=0}^{M-1}e^{j2\pi(\frac{l-l'}{M\Delta f}-\tau_i)m'\Delta f}\,. \tag{3-76}$$

By substituting (3-14) into (3-76), we obtain

$$\mathcal{F}^{IDI}\left(\frac{l-l'}{M\Delta f},\frac{l_{\tau_i}+\iota_{\tau_i}}{M\Delta f}\right)=\sum_{m'=0}^{M-1}e^{j\frac{2\pi}{M}\left(l-l'-l_{\tau_i}-\iota_{\tau_i}\right)m'}\,. \tag{3-77}$$

Since the number of subcarriers M is usually very large in practical OTFS systems, the delay resolution can be increased at high precision to ignore the impact of fractional delay. Therefore, by substituting $l_{\tau_i} = 0$ into equation (3-77), we have

$$\mathcal{F}^{IDI}\left(\frac{l-l'}{M\Delta f}, \frac{l_{\tau_i}}{M\Delta f}\right) = \sum_{m'=0}^{M-1} e^{j\frac{2\pi}{M}\left(l-l'-l_{\tau_i}\right)m'}, \tag{3-78}$$

The term $e^{j\frac{2\pi}{M}\left(l-l'-l_{\tau_i}\right)m'}$ in equation (3-78) can be considered as a geometric sequence with the index m', hence we sum up all the terms of m' from 0 to M-1 and obtain

$$\mathcal{F}^{IDI}\left(\frac{l-l'}{M\Delta f}, \frac{l_{\tau_i}}{M\Delta f}\right) = \frac{e^{j2\pi(l-l'-l_{\tau_i})}-1}{e^{j\frac{2\pi}{M}(l-l'-l_{\tau_i})}-1} = \begin{cases} M & ,\left[l-l'-l_{\tau_i}\right]_M = 0 \\ 0 & ,otherwise \end{cases}, \tag{3-79}$$

We then evaluate $\mathcal{G}^{IDI}(\nu, \nu_i)$ at $\nu = \frac{k-k'}{NT}$ as

$$\mathcal{G}^{IDI}\left(\frac{k-k'}{NT}, \nu_i\right) = \sum_{n'=0}^{N-1} e^{-j2\pi\left(\frac{k-k'}{NT}-\nu_i\right)n'T}. \tag{3-80}$$

By substituting (3-15) into (3-80), we obtain

$$\mathcal{G}^{IDI}\left(\frac{k-k'}{NT}, \frac{k_{\nu_i}+\kappa_{\nu_i}}{NT}\right) = \sum_{n'=0}^{N-1} e^{-j\frac{2\pi}{N}\left(k-k'-k_{\nu_i}-\kappa_{\nu_i}\right)n'}. \tag{3-81}$$

Similarly, the right side of the equation (3-81) can be seen as the summation of a geometric sequence

$$\mathcal{G}^{IDI}\left(\frac{k-k'}{NT}, \frac{k_{\nu_i}+\kappa_{\nu_i}}{NT}\right) = \frac{e^{-j2\pi(k-k'-k_{\nu_i}-\kappa_{\nu_i})}-1}{e^{-j\frac{2\pi}{N}(k-k'-k_{\nu_i}-\kappa_{\nu_i})}-1}. \tag{3-82}$$

Due to the fractional κ_{ν_i}, for a given k, $\mathcal{G}^{IDI}\left(\frac{k-k'}{NT}, \frac{k_{\nu_i}+\kappa_{\nu_i}}{NT}\right) \neq 0$ for all k'. We define $\theta \triangleq -\frac{\pi}{N}\left(k-k'-k_{\nu_i}-\kappa_{\nu_i}\right)$ and hence get

$$\left|\frac{1}{N}\mathcal{G}^{IDI}\left(\frac{k-k'}{NT}, \nu_i\right)\right| = \left|\frac{\sin\left(N\theta\right)}{N\sin\left(\theta\right)}\right|. \tag{3-83}$$

By equation $\sin\left(\alpha+\beta\right) = \sin\left(\alpha\right)\cos\left(\beta\right)+\cos\left(\alpha\right)\sin\left(\beta\right)$, we have

$$\left|\frac{\sin\left(N\theta\right)}{N\sin\left(\theta\right)}\right| = \left|\frac{\sin\left(\left(N-1\right)\theta\right)\cos\left(\theta\right)+\sin\left(\theta\right)\cos\left(\left(N-1\right)\theta\right)}{N\sin\left(\theta\right)}\right|. \tag{3-84}$$

Through inequality $|a+b| \le |a|+|b|$ and $|\sin(N\theta)| \le N|\sin(\theta)|$, which can be proved by induction, we obtain the following inequality relationship

$$\left|\frac{\sin\left((N-1)\theta\right)\cos\left(\theta\right)+\sin\left(\theta\right)\cos\left((N-1)\theta\right)}{N\sin\left(\theta\right)}\right| \le \frac{N-1}{N}\left|\cos\left(\theta\right)\right|+\frac{1}{N}. \quad (3\text{-}85)$$

From the inequality, when both sides are close to 1, the upper bound is tight for small values of θ. Also it has a peak at the nearest value of θ when $k' = k - k_{v_i}$. Due to k' moving away from $k - k_{v_i}$, the upper bound decreases approximately with the slope of $\frac{\pi}{N}\left(k-k'-k_{v_i}-\kappa_{v_i}\right)$ while $|\theta|$ increases. Since N is quite large in the practical OTFS system, the function decreases rapidly.

From the above analysis, we can consider only a small number $2N_i+1$, for some $N_i > 0$, of significant values of $\mathcal{G}^{IDI}\left(\frac{k-k'}{NT}, \frac{k_{v_i}+\kappa_{v_i}}{NT}\right)$ around the peak $k-k_{v_i}$, i.e., $\left[k-k_{v_i}-N_i\right] \le k' \le \left[k-k_{v_i}+N_i\right]$, where $N_i \ll N$. By using this approximation and substituting (3-73), (3-79), and (3-82) into (3-70), the received signal $\mathrm{y}_{DD}[k,l]$ now can be written as

$$\mathrm{y}_{DD}[k,l] \approx \sum_{i=1}^{P} \sum_{k'=[k-k_{v_i}-N_i]_N}^{[k-k_{v_i}+N_i]_N} \left(\frac{e^{-j2\pi(k-k_{v_i}-k'-\kappa_{v_i})}-1}{Ne^{-j\frac{2\pi}{N}(k-k_{v_i}-k'-\kappa_{v_i})}-N}\right) h_i e^{-j2\pi v_i \tau_i}$$

$$\times\, x_{DD}\left[k',[l-l_{\tau_i}]_M\right] + w_{DD}\left[k,l\right]. \quad (3\text{-}86)$$

By substituting $k' = \left(k-k_{v_i}+q\right)$ into equation (3-86), the expression form of the approximated input-output relation in the DD domain for ideal pulses is finally obtained by

$$y_{DD}\left[k,l\right] \approx \sum_{i=1}^{P} \sum_{q=-N_i}^{N_i} \left(\frac{e^{-j2\pi(-q-\kappa_{v_i})}-1}{Ne^{-j\frac{2\pi}{N}(-q-\kappa_{v_i})}-N}\right) h_i e^{-j2\pi v_i \tau_i}$$

$$\times x_{DD}\left[[k-k_{\nu_i}+q]_N,[l-l_{\tau_i}]_M\right]+w_{DD}\left[k,l\right]. \tag{3-87}$$

From equation (3-87), the approximated received $y_{DD}[k,l]$ can be seen as the linear combination of $S=\sum_{i=1}^{P}2N_i+1$ transmitted signals. Out of 2Ni + 1 transmitted signals in the ith path, the signal corresponding to q = 0, $x_{DD}\left[[k-k_{\nu_i}]_N,[l-l_{\tau_i}]_M\right]$ contributes the most and all the other $2N_i$ signals can be seen as interference, which is called inter-Doppler interference (IDI). Further, the number of transmitted signals S affecting the received signal $y_{DD}[k,l]$ in equation (3-87) is much smaller than MN in equation (3-70).

The input-output relation in the DD domain for ideal pulses can be simplified for some special cases. For the ideal channel, where we assume $h(\tau,\nu)=\delta(\tau)\delta(\nu)$, the received signal can be written as

$$y_{DD}[k,l]=x_{DD}[k,l]+w_{DD}\left[k,l\right], \tag{3-88}$$

which is consistent with the transmitted signal and behaves like an AWGN channel.

For the case without fractional Doppler, where we assume $\kappa_{\nu_i}=0,\forall i$, the received signal in equation (3-84) can be obtained by replacing $N_i=0$

$$y_{DD}[k,l]=\sum_{i=1}^{P}h_i e^{-j2\pi\nu_i\tau_i}x_{DD}[[k-k_{\nu_i}]_N,[l-l_{\tau_i}]_M]+w_{DD}\left[k,l\right]. \tag{3-89}$$

For each path, the transmitted signal is circularly shifted by the delay and Doppler taps and scaled by the associated channel gain.

3.3.3 Input-Output Relation in DD Domain for Rectangular Pulses

In section 3.2.3, we show the TF domain input-output relation in equation (3-52). To get the DD domain input-output relation for rectangular pulses, we do SFFT to (3-

52), and hence obtain

$$\mathrm{y}_{DD}\left[k,l\right]=\mathrm{y}_{DD}^{ICI}\left[k,l\right]+\mathrm{y}_{DD}^{ISI}\left[k,l\right]+w_{DD}\left[k,l\right], \tag{3-90}$$

where

$$\mathrm{y}_{DD}^{ICI}\left[k,l\right]=\frac{1}{\sqrt{NM}}\sum_{n=0}^{N-1}\sum_{m=0}^{M-1}\left(\sum_{m'=0}^{M-1}H_{n,m}\left[n,m'\right]X_{TF}\left[n,m'\right]\right)e^{-j2\pi\left(\frac{nk}{N}-\frac{ml}{M}\right)}, \tag{3-91}$$

$$\mathrm{y}_{DD}^{ISI}\left[k,l\right]=\frac{1}{\sqrt{NM}}\sum_{n=0}^{N-1}\sum_{m=0}^{M-1}\left(\sum_{m'=0}^{M-1}H_{n,m}\left[n-1,m'\right]X_{TF}\left[n-1,m'\right]\right)e^{-j2\pi\left(\frac{nk}{N}-\frac{ml}{M}\right)}, \tag{3-92}$$

$$w_{DD}\left[k,l\right]=\frac{1}{\sqrt{NM}}\sum_{n=0}^{N-1}\sum_{m=0}^{M-1}W_{TF}\left[n,m\right]e^{-j2\pi\left(\frac{nk}{N}-\frac{ml}{M}\right)}. \tag{3-93}$$

3.3.3.1 ICI Analysis in DD Domain for Rectangular Pulses

For the ICI term $\mathrm{y}_{DD}^{ICI}\left[k,l\right]$ in (3-90), we do SFFT (3-33) to $X_{TF}\left[n,m'\right]$ and reorganize the terms, hence we obtain

$$\mathrm{y}_{DD}^{ICI}\left[k,l\right]=\frac{1}{NM}\sum_{k'=0}^{N-1}\sum_{l'=0}^{M-1}x_{DD}\left[k',l'\right]h_{k,l}^{ICI}\left[k',l'\right], \tag{3-94}$$

where

$$h_{k,l}^{ICI}\left[k',l'\right]=\sum_{n=0}^{N-1}\sum_{m=0}^{M-1}\sum_{m'=0}^{M-1}H_{n,m}\left[n,m'\right]e^{-j2\pi n\left(\frac{k-k'}{N}\right)}e^{j2\pi\left(\frac{ml-m'l'}{M}\right)}. \tag{3-95}$$

By substituting (3-41) and (3-27) into (3-95), we obtain

$$h_{k,l}^{ICI}\left[k',l'\right]=\sum_{i=1}^{P}h_i\mathcal{G}^{ICI}(\nu_i)\mathcal{F}^{ICI}(\tau_i,\nu_i), \tag{3-96}$$

where

$$\mathcal{G}^{ICI}(\nu_i)=\sum_{n=0}^{N-1}e^{-j2\pi n\left(\frac{k-k'-k_{\nu_i}-\kappa_{\nu_i}}{N}\right)}, \tag{3-97}$$

$$\mathcal{F}^{ICI}(\tau_i,\nu_i)=\frac{1}{M}\sum_{p=0}^{M-1-l_{r_i}}e^{j2\pi\frac{p}{M}\left(\frac{k_{r_i}+n_{r_i}}{N}\right)}\sum_{m=0}^{M-1}e^{-j2\pi(p+l_{r_i}-l)\frac{m}{M}}\sum_{m'=0}^{M-1}e^{j2\pi(p-l')\frac{m'}{M}} \tag{3-98}$$

$$=M\sum_{p=0}^{M-1-l_{\tau_i}}e^{j2\pi\frac{p}{M}\left(\frac{k_{\nu_i}+\kappa_{\nu_i}}{N}\right)}\delta\left(\left[p+l_{\tau_i}-l\right]_M\right)\delta\left(\left[p-l'\right]_M\right)\cdot \tag{3-99}$$

Hence, by substituting (3-96), (3-97), and (3-99) into (3-94), the ICI term $\mathrm{y}_{DD}^{ICI}[k,l]$ can be approximated as

$$\mathrm{y}_{DD}^{ICI}[k,l] \approx \frac{1}{N}\sum_{i=1}^{P} h_i \left[\sum_{p=0}^{M-1-l_{\tau_i}} e^{j2\pi\frac{p}{M}\left(\frac{k_{\nu_i}+\kappa_{\nu_i}}{N}\right)} \delta\left(\left[p+l_{\tau_i}-l\right]_M\right) \right.$$

$$\left. \times \sum_{q=-N_i}^{N_i} \left(\frac{-e^{j2\pi\left(-q-\kappa_{\nu_i}\right)}-1}{e^{-j\frac{2\pi}{N}\left(-q-\kappa_{\nu_i}\right)}-1} \right) x_{DD}\left[\left[k-k_{\nu_i}+q\right]_N, p\right] \right]. \quad (3\text{-}100)$$

From (3-100), we can observe that it is non-zero only if the following condition is satisfied

$$p = [l-l_{\tau_i}]_M \text{ and } 0 \le p \le M-1-l_{\tau_i}. \quad (3\text{-}101)$$

Therefore, conditions (3-101) are satisfied only if $l \ge l_{\tau_i}$ and $p = l - l_{\tau_i}$. Finally, with the conditions on l and p, the following approximation can be obtained

$$\mathrm{y}_{DD}^{ICI}[k,l]$$

$$\approx \begin{cases} \sum_{i=1}^{P}\sum_{q=-N_i}^{N_i} h_i \left[\frac{1}{N}\beta_i(q)\right] e^{j2\pi\left(\frac{l-l_{\tau_i}}{M}\right)\left(\frac{k_{\nu_i}+\kappa_{\nu_i}}{N}\right)} x_{DD}\left[[k-k_{\nu_i}+q]_N, [l-l_{\tau_i}]_M\right] & , l \ge l_{\tau_i} \\ 0 & , else \end{cases}, \quad (3\text{-}102)$$

where we define

$$\beta_i(q) = \frac{e^{-j2\pi(-q-\kappa_{\nu_i})}-1}{e^{-j\frac{2\pi}{N}(-q-\kappa_{\nu_i})}-1}. \quad (3\text{-}103)$$

3.3.3.2 ISI Analysis in DD Domain for Rectangular Pulses

For the ISI term $\mathrm{y}_{DD}^{ISI}[k,l]$ in equation (3-90), similarly to $\mathrm{y}_{DD}^{ICI}[k,l]$,we also do SFFT (3-33) to $X_{TF}[n-1,m']$ and reorganize the terms, hence we obtain

$$\mathrm{y}_{DD}^{ISI}[k,l] = \frac{1}{NM}\sum_{k'=0}^{N-1}\sum_{l'=0}^{M-1} e^{-j2\pi\frac{k'}{N}} x_{DD}[k',l'] h_{k,l}^{ISI}[k',l'], \quad (3\text{-}104)$$

where we define

$$h_{k,l}^{ISI}[k',l'] \triangleq \sum_{n=0}^{N-1}\sum_{m=0}^{M-1}\sum_{m'=0}^{M-1} H_{n,m}[n-1,m'] e^{-j2\pi n\left(\frac{k-k'}{N}\right)} e^{j2\pi\left(\frac{ml-m'l'}{N}\right)}. \quad (3\text{-}105)$$

By substituting the value of $H_{n,m}\left[n-1,m'\right]$ from (3-41) and cross-ambiguity function in (3-7), $h_{k,l}^{ISI}\left[k',l'\right]$ can be written as

$$h_{k,l}^{ISI}\left[k',l'\right]=\sum_{i=0}^{P}h_i\mathcal{G}^{ISI}(\nu_i)\mathcal{F}^{ISI}(\tau_i,\nu_i), \tag{3-106}$$

where

$$\mathcal{G}^{ISI}(\nu_i)=\sum_{n=1}^{N-1}e^{-j2\pi n\left(\frac{k-k'-k_{\nu_i}-\kappa_{\nu_i}}{N}\right)}, \tag{3-107}$$

$$\mathcal{F}^{ISI}(\tau_i,\nu_i)=\frac{1}{M}\sum_{p=M-l_{\tau_i}}^{M-1}e^{-j2\pi\left(\frac{p-M}{M}\right)}e^{-j2\pi n\left(\frac{k_{\nu_i}+\kappa_{\nu_i}}{N}\right)}\sum_{m=0}^{M-1}e^{-j2\pi\left(p+l_{\tau_i}-l+M\right)\frac{m}{M}}\sum_{m'=0}^{M-1}e^{-j2\pi\left(p-l'\right)\frac{m'}{M}}, \tag{3-108}$$

Due to equation (3-107), the summation n starts from 1 as the first symbol that does not have any previous symbol to experience ISI. Therefore, by using the value $\mathcal{G}^{ISI}(\nu_i)=\mathcal{G}^{ICI}(\nu_i)-1$, $\mathrm{y}_{DD}^{ISI}\left[k,l\right]$ can be approximated as

$$\begin{aligned}\mathrm{y}_{DD}^{ISI}\left[k,l\right]\approx\frac{1}{N}\sum_{i=1}^{P}h_i\Bigg[&\sum_{p=M-l_{\tau_i}}^{M-1}e^{j2\pi\left(\frac{p-M}{M}\right)\left(\frac{k_{\nu_i}+\kappa_{\nu_i}}{N}\right)}\delta\left(\left[p+l_{\tau_i}-l\right]_M\right)\Bigg\{\sum_{q=-N_i}^{N_i}\left(\beta_i(q)-1\right)\\&\times e^{-j2\pi\frac{\left[k-k_{\nu_i}+q\right]_N}{N}}x_{DD}\left[\left[k-k_{\nu_i}+q\right]_N,p\right]\sum_{\substack{k'=0,\\k'\neq[k-k_{\nu_i}+q],\,q=[-N_i,N_i]}}^{N-1}e^{-j2\pi\frac{k'}{N}}x_{DD}\left[k',p\right]\Bigg\}\Bigg].\end{aligned} \tag{3-109}$$

By neglecting the signals $x\left[k',p\right]$ for $k'\neq\left[k-k_{\nu_i}+q\right]_N, q\in\left[-N_i,N_i\right]$, due to their very small coefficients for practical values of N(e.g., $N=64,\ 128$), the approximation of $\mathrm{y}_{DD}^{ISI}\left[k,l\right]$ in (3-109) can be simplified as

$$\begin{aligned}\mathrm{y}_{DD}^{ISI}\left[k,l\right]\approx\frac{1}{N}\sum_{i=1}^{P}h_i\Bigg[&\sum_{p=M-l_{\tau_i}}^{M-1}e^{j2\pi\left(\frac{p-M}{M}\right)\left(\frac{k_{\nu_i}+\kappa_{\nu_i}}{N}\right)}\delta\left(\left[p+l_{\tau_i}-l\right]_M\right)\\&\times\sum_{q=-N_i}^{N_i}\left(\beta_i(q)-1\right)e^{-j2\pi\frac{\left[k-k_{\nu_i}+q\right]_N}{N}}x_{DD}\left[\left[k-k_{\nu_i}+q\right]_N,p\right]\Bigg].\end{aligned} \tag{3-110}$$

Therefore, the value of (3-110) is non-zero if the following conditions are satisfied

$$p=[l-l_{\tau_i}]_M \text{ and } M-l_{\tau_i} \le p \le M-1. \tag{3-111}$$

Therefore, conditions (3-108) are satisfied only if $l<l_{\tau_i}$ and $p=l-l_{\tau_i}+M$. Finally, with the conditions on l and p, the following approximation is obtained

$$\mathrm{y}_{DD}^{ISI}\left[k,l\right]\approx$$
$$\begin{cases} \sum_{i=1}^{P}\sum_{q=-N_i}^{N_i} h_i\left[\frac{1}{N}\left(\beta_i\left(q\right)-1\right)\right]e^{-j2\pi\frac{\left[k-k_{\nu_i}+q\right]_N}{N}} x_{DD}\left[\left[k-k_{\nu_i}+q\right]_N,\left[l-l_{\tau_i}\right]_M\right] & ,l<l_{\tau_i} \\ 0 & ,else, \end{cases} \tag{3-112}$$

where $\beta_i\left(q\right)$ has been declared in (3-100).

From (3-102) and (3-112), the overall expression of the DD domain input-output relation for rectangular pulses is obtained by

$$y_{DD}[k,l]\approx$$
$$\sum_{i=1}^{P}\sum_{q=-N_i}^{N_i} h_i e^{j2\pi\left(\frac{l-l_{r_i}}{M}\right)\left(\frac{k_{\nu_i}+\kappa_{\nu_i}}{N}\right)}\alpha_i(k,l,q)x_{DD}\left[[k-k_{\nu_i}+q]_N,[l-l_{\tau_i}]_M\right]+w_{DD}\left[k,l\right], \tag{3-113}$$

where

$$\alpha_i(k,l,q)=\begin{cases} \frac{1}{N}\beta_i(q) & ,l_{\tau_i}\le l<M \\ \frac{1}{N}\left(\beta_i(q)-1\right)e^{-j2\pi\frac{[k-k_{\tau_i}+q]_N}{N}} & ,0\le l<l_{\tau_i} \end{cases}. \tag{3-114}$$

The input-output relation in the DD domain for rectangular pulses can be simplified for some special cases. For the ideal channel, where we assume $h(\tau,\nu)=\delta(\tau)\delta(\nu)$, the received signal can be written as

$$y_{DD}[k,l]=x_{DD}[k,l]+w_{DD}\left[k,l\right], \tag{3-115}$$

which shows the same result as the condition of ideal pulses.

For the case without fractional Doppler, where we assume $\kappa_{\nu_i}=0,\forall i$, the received signal in equation (3-113) can be simplified to

$$y_{DD}[k,l] \approx \sum_{i=1}^{P} h_i e^{j2\pi\left(\frac{l-l_{\tau_i}}{M}\right)\frac{k_{\nu_i}}{N}} \alpha_i(k,l) x\Big[[k-k_{\nu_i}]_N, [l-l_{\tau_i}]_M\Big] + w_{DD}\big[k,l\big], \quad (3\text{-}116)$$

where

$$\alpha_i(k,l) = \begin{cases} 1 & l_{\tau_i} \le l < M \\ \dfrac{N-1}{N} e^{-j2\pi\left(\frac{[k-k_{\nu_i}]_N}{N}\right)} & 0 \le l < l_{\tau_i} \end{cases}, \quad (3\text{-}117)$$

For the above special channel model cases, IDI does not appear.

Moreover, from (3-60), (3-60), and (3-62), the matrix form of the input-output relation in the DD domain for rectangular pulses corresponding to the equation (3-113) is obtained by substituting the transceiver matrices with identity matrices

$$\mathbf{y}_{DD} = \mathbf{H}_{DD}^{rect} \mathbf{x}_{DD} + \mathbf{w}_{DD}, \quad (3\text{-}118)$$

where

$$\mathbf{w}_{DD} = (\mathbf{F}_N \otimes \mathbf{I}_M)\mathbf{w}_T, \quad (3\text{-}119)$$

$$\mathbf{H}_{DD}^{rect} = (\mathbf{F}_N \otimes \mathbf{I}_M)\mathbf{H}_T(\mathbf{F}_N^H \otimes \mathbf{I}_M). \quad (3\text{-}120)$$

3.4 Equalization

OTFS system channel equalization methods are mainly divided into linear equalization and nonlinear equalization. The advantage of the linear equalization algorithm is its low computational complexity. The linear equalization algorithm mainly includes the ZF algorithm and MMSE algorithm, which we will introduce in section 3.4. Moreover, we will prove the equivalence of the ZF algorithm between time domain equalization and DD domain equalization for rectangular pulses, as well as the MMSE algorithm, which will be verified by simulation in section 3.5.

3.4.1 ZF Equalization

The purpose of the ZF algorithm is to minimize the $\|\mathbf{y}-\mathbf{Hx}\|^2$ by forcing inter-channel interference to be zero. Hence, we obtain the input-output relation of the ZF equalizer in the time domain

$$\mathbf{r}_T^{ZF}=\mathbf{G}_T^{ZF}\mathbf{r}_T\cdot \tag{3-121}$$

where $\mathbf{r}_T^{ZF}$ and $\mathbf{G}_T^{ZF}$ denote the output and equalization matrix of the ZF equalizer in the time domain, respectively. In the SISO communication system, the time domain equalization matrix for the ZF algorithm is given by

$$\mathbf{G}_T^{ZF}=\mathbf{H}_T^{-1}\cdot \tag{3-122}$$

Similarly, we obtain the input-output relation of the ZF equalizer in the DD domain

$$\mathbf{y}_{DD}^{ZF}=\mathbf{G}_{DD}^{ZF}\mathbf{y}_{DD}, \tag{3-123}$$

where $\mathbf{y}_{DD}^{ZF}$ and $\mathbf{G}_{DD}^{ZF}$ are denoted as the output and equalization matrix of the ZF equalizer in the DD domain. For rectangular pulses, the DD domain equalization matrix for the ZF algorithm is given by

$$\mathbf{G}_{DD}^{ZF}=(\mathbf{H}_{DD}^{rect})^{-1}\cdot \tag{3-124}$$

In the following, we will prove the equivalence of the ZF algorithm between time domain equalization and DD domain equalization for rectangular pulses by deriving (3-123) from (3-121). By substituting the time domain input-output relation (3-24) into (3-121), we obtain

$$\mathbf{r}_T^{ZF}=\mathbf{G}_T^{ZF}(\mathbf{H}_T\mathbf{s}_T+\mathbf{w}_T)\cdot \tag{3-125}$$

By substituting $\mathbf{G}_T^{ZF}=\mathbf{H}_T^{-1}$ into (3-125), we obtain

$$\mathbf{r}_T^{ZF}=\mathbf{s}_T+\mathbf{H}_T^{-1}\mathbf{w}_T\cdot \tag{3-126}$$

Then, we multiply $(\mathbf{F}_N\otimes\mathbf{I}_M)$ on both sides of the equation (3-126), and hence get

$$\begin{aligned}(\mathbf{F}_N\otimes\mathbf{I}_M)\mathbf{r}_T^{ZF} &= (\mathbf{F}_N\otimes\mathbf{I}_M)(\mathbf{s}_T+\mathbf{H}_T^{-1}\mathbf{w}_T)\\ &=(\mathbf{F}_N\otimes\mathbf{I}_M)\mathbf{s}_T+(\mathbf{F}_N\otimes\mathbf{I}_M)\mathbf{H}_T^{-1}\mathbf{w}_T\ .\end{aligned} \tag{3-127}$$

By substituting $\mathbf{y}_{DD}^{ZF}=(\mathbf{F}_N\otimes\mathbf{I}_M)\mathbf{r}_T^{ZF}$ into (3-127), we obtain

$$\mathbf{y}_{DD}^{ZF}=(\mathbf{F}_N\otimes\mathbf{I}_M)\mathbf{s}_T+(\mathbf{F}_N\otimes\mathbf{I}_M)\mathbf{H}_T^{-1}\mathbf{w}_T\cdot \tag{3-128}$$

By substituting $\mathbf{s}_T=(\mathbf{F}_N^H\otimes\mathbf{I}_M)\mathbf{x}_{DD}$ into (3-128), we have

$$\mathbf{y}_{DD}^{ZF}=(\mathbf{F}_N\otimes\mathbf{I}_M)(\mathbf{F}_N^H\otimes\mathbf{I}_M)\mathbf{x}_{DD}+(\mathbf{F}_N\otimes\mathbf{I}_M)\mathbf{H}_T^{-1}\mathbf{w}_T\cdot \tag{3-129}$$

Due to the property of Kronecker product $(\mathbf{F}_N\otimes\mathbf{I}_M)(\mathbf{F}_N^H\otimes\mathbf{I}_M)=\mathbf{I}_{MN}$, we obtain

$$\mathbf{y}_{DD}^{ZF}=\mathbf{x}_{DD}+(\mathbf{F}_N\otimes\mathbf{I}_M)\mathbf{H}_T^{-1}\mathbf{w}_T\cdot \tag{3-130}$$

By substituting $\mathbf{w}_T=(\mathbf{F}_N^H\otimes\mathbf{I}_M)\mathbf{w}_{DD}$ into (3-130), we obtain

$$\begin{aligned}\mathbf{y}_{DD}^{ZF}&=\mathbf{x}_{DD}+(\mathbf{F}_N\otimes\mathbf{I}_M)\mathbf{H}_T^{-1}(\mathbf{F}_N^H\otimes\mathbf{I}_M)\mathbf{w}_{DD}\\ &=\mathbf{x}_{DD}+\left[(\mathbf{F}_N\otimes\mathbf{I}_M)\mathbf{H}_T(\mathbf{F}_N^H\otimes\mathbf{I}_M)\right]^{-1}\mathbf{w}_{DD}\ .\end{aligned} \tag{3-131}$$

We observe that $(\mathbf{F}_N\otimes\mathbf{I}_M)\mathbf{H}_T(\mathbf{F}_N^H\otimes\mathbf{I}_M)$ in (3-131) is equal to the DD domain effective channel matrix for rectangular pulses (3-120), hence we get

$$\begin{aligned}\mathbf{y}_{DD}^{ZF}&=\mathbf{x}_{DD}+(\mathbf{H}_{DD}^{rect})^{-1}\mathbf{w}_{DD}\\ &=(\mathbf{H}_{DD}^{rect})^{-1}(\mathbf{H}_{DD}^{rect}\mathbf{x}_{DD}+\mathbf{w}_{DD})\ .\end{aligned} \tag{3-132}$$

By substituting (3-118) into (3-132), we obtain the input-output relation of the ZF equalizer in the DD domain

$$\mathbf{y}_{DD}^{ZF}=(\mathbf{H}_{DD}^{rect})^{-1}\mathbf{y}_{DD}, \tag{3-133}$$

which is equivalent to (3-123) due to $\mathbf{G}_{DD}^{ZF}=(\mathbf{H}_{DD}^{rect})^{-1}$. Hence, the equivalence of the ZF algorithm between time domain equalization and DD domain equalization for rectangular pulses is proved.

Though the ZF equalizer can eliminate the interference between the data streams and the receivers, the effect of noise is amplified due to the non-orthogonality of the ZF equalization matrix $\boldsymbol{G}^{ZF}$. Especially, when the data volume, as well as the scale of the antenna array, is very large, the performance of the ZF equalization may significantly degrade.

3.4.2 MMSE Equalization

The MMSE equalization algorithm is widely to mitigate the effect of channel distortion in communication systems. Different from the ZF algorithm, the MMSE algorithm addresses the issue of noise amplification, when the signal-to-noise ratio (SNR) is low. The purpose of the MMSE algorithm is to suppress the impact of noise by minimizing $E\left\{\|\hat{\boldsymbol{x}}-\boldsymbol{x}\|^2\right\}$. Due to the principle of orthogonality, the minimum estimated value is obtained when $E\left\{\boldsymbol{y}(\boldsymbol{x}-\hat{\boldsymbol{x}})^{\mathrm{H}}\right\}=0$. The time domain equalization matrix for the MMSE algorithm is given by

$$\mathbf{G}_T^{MMSE}=(\mathbf{H}_T\mathbf{H}_T^H+\frac{1}{\rho}\mathbf{I}_{MN})^{-1}\mathbf{H}_T^H, \tag{3-134}$$

where ρ denotes the average SNR. Hence, the time domain input-output relation for the MMSE equalizer is obtained

$$\mathbf{r}_T^{ZF}=\mathbf{G}_T^{MMSE}\mathbf{r}_T. \tag{3-135}$$

Similarly, we have the DD domain input-output relation for the MMSE equalizer, as shown in the following

$$\mathbf{y}_{DD}^{ZF}=\mathbf{G}_{DD}^{MMSE}\mathbf{y}_{DD}, \tag{3-136}$$

where

$$\mathbf{G}_{DD}^{MMSE}=\left[\mathbf{H}_{DD}^{rect}(\mathbf{H}_{DD}^{rect})^H+\frac{1}{a}\mathbf{I}_{MN}\right]^{-1}(\mathbf{H}_{DD}^{rect})^H. \tag{3-137}$$

Similar to the ZF equation algorithm, we will prove the equivalence of the ZF algorithm between time domain equalization and DD domain equalization for rectangular pulses by deriving (3-135) from (3-136). Firstly, by substituting the time domain input-output relation (3-24) into (3-135), we obtain

$$\mathbf{r}_T^{ZF} = \mathbf{G}_T^{MMSE}(\mathbf{H}_T\mathbf{s}_T + \mathbf{w}_T)\cdot \tag{3-138}$$

By multiplying $(\mathbf{F}_N \otimes \mathbf{I}_M)$ on both sides of the equation (3-138), we get

$$(\mathbf{F}_N \otimes \mathbf{I}_M)\mathbf{r}_T^{ZF} = (\mathbf{F}_N \otimes \mathbf{I}_M)\mathbf{G}_T^{MMSE}(\mathbf{H}_T\mathbf{s}_T + \mathbf{w}_T)\cdot \tag{3-139}$$

Due to $\mathbf{y}_{DD}^{ZF} = (\mathbf{F}_N \otimes \mathbf{I}_M)\mathbf{r}_T^{ZF}$, we have

$$\mathbf{y}_{DD}^{ZF} = (\mathbf{F}_N \otimes \mathbf{I}_M)\mathbf{G}_T^{MMSE}(\mathbf{H}_T\mathbf{s}_T + \mathbf{w}_T)\cdot \tag{3-140}$$

By substituting (3-134) into (3-140), we obtain

$$\mathbf{y}_{DD}^{ZF} = (\mathbf{F}_N \otimes \mathbf{I}_M)\left[(\mathbf{H}_T\mathbf{H}_T^H + \frac{1}{\rho}\mathbf{I}_{MN})^{-1}\mathbf{H}_T^H\right](\mathbf{H}_T\mathbf{s}_T + \mathbf{w}_T)\cdot \tag{3-141}$$

By substituting $s_T = (\mathbf{F}_N^H \otimes \mathbf{I}_M)\mathbf{x}_{DD}$ and $\mathbf{w}_T = (\mathbf{F}_N^H \otimes \mathbf{I}_M)\mathbf{w}_{DD}$ into (3-141), we can get

$$\begin{aligned}\mathbf{y}_{DD}^{ZF} &= (\mathbf{F}_N \otimes \mathbf{I}_M)(\mathbf{H}_T\mathbf{H}_T^H + \frac{1}{\rho}\mathbf{I}_{MN})^{-1}\mathbf{H}_T^H\mathbf{H}_T(\mathbf{F}_N^H \otimes \mathbf{I}_M)\mathbf{x}_{DD} \\ &+ (\mathbf{F}_N \otimes \mathbf{I}_M)(\mathbf{H}_T\mathbf{H}_T^H + \frac{1}{\rho}\mathbf{I}_{MN})^{-1}\mathbf{H}_T^H(\mathbf{F}_N^H \otimes \mathbf{I}_M)\mathbf{w}_{DD}.\end{aligned} \tag{3-142}$$

Due to $(\mathbf{F}_N^H \otimes \mathbf{I}_M)(\mathbf{F}_N \otimes \mathbf{I}_M) = \mathbf{I}_{MN}$ and, we have

$$\begin{aligned}\mathbf{y}_{DD}^{ZF} &= \left[(\mathbf{F}_N \otimes \mathbf{I}_M)(\mathbf{H}_T\mathbf{H}_T^H + \frac{1}{\rho}\mathbf{I}_{MN})^{-1}\mathbf{H}_T^H(\mathbf{F}_N^H \otimes \mathbf{I}_M)\right]\left[(\mathbf{F}_N \otimes \mathbf{I}_M)\mathbf{H}_T(\mathbf{F}_N^H \otimes \mathbf{I}_M)\right] \\ \mathbf{x}_{DD} &+ \left[(\mathbf{F}_N \otimes \mathbf{I}_M)(\mathbf{H}_T\mathbf{H}_T^H + \frac{1}{\rho}\mathbf{I}_{MN})^{-1}(\mathbf{F}_N^H \otimes \mathbf{I}_M)\right]\left[(\mathbf{F}_N \otimes \mathbf{I}_M)\mathbf{H}_T^H(\mathbf{F}_N^H \otimes \mathbf{I}_M)\right]\mathbf{w}_{DD}.\end{aligned} \tag{3-143}$$

We observe that $(\mathbf{F}_N \otimes \mathbf{I}_M)\mathbf{H}_T(\mathbf{F}_N^H \otimes \mathbf{I}_M)$ and $(\mathbf{F}_N \otimes \mathbf{I}_M)\mathbf{H}_T^H(\mathbf{F}_N^H \otimes \mathbf{I}_M)$ in (3-143) are equal to the DD domain effective channel matrix for rectangular pulses (3-120) and its transpose, respectively. Hence we can get

$$\begin{aligned}\mathbf{y}_{DD}^{ZF} &= \left[(\mathbf{F}_N \otimes \mathbf{I}_M)(\mathbf{H}_T\mathbf{H}_T^H + \frac{1}{\rho}\mathbf{I}_{MN})^{-1}\mathbf{H}_T^H(\mathbf{F}_N^H \otimes \mathbf{I}_M) \right]\mathbf{H}_{DD}^{rect}\mathbf{x}_{DD} \\ &+ \left[(\mathbf{F}_N \otimes \mathbf{I}_M)(\mathbf{H}_T\mathbf{H}_T^H + \frac{1}{\rho}\mathbf{I}_{MN})^{-1}(\mathbf{F}_N^H \otimes \mathbf{I}_M) \right](\mathbf{H}_{DD}^{rect})^H\mathbf{w}_{DD}.\end{aligned} \tag{3-144}$$

Then, by the property of the inverse matrix $\left(\mathbf{ABC}\right)^{-1} = \mathbf{C}^{-1}\mathbf{B}^{-1}\mathbf{A}^{-1}$, equation (3-144) can be written as

$$\begin{aligned}\mathbf{y}_{DD}^{ZF} &= \left[(\mathbf{F}_N \otimes \mathbf{I}_M)(\mathbf{H}_T\mathbf{H}_T^H + \frac{1}{\rho}\mathbf{I}_{MN})\mathbf{H}_T^H(\mathbf{F}_N^H \otimes \mathbf{I}_M) \right]^{-1}\mathbf{H}_{DD}^{rect}\mathbf{x}_{DD} \\ &+ \left[(\mathbf{F}_N \otimes \mathbf{I}_M)(\mathbf{H}_T\mathbf{H}_T^H + \frac{1}{\rho}\mathbf{I}_{MN})^{-1}(\mathbf{F}_N^H \otimes \mathbf{I}_M) \right]^{-1}(\mathbf{H}_{DD}^{rect})^H\mathbf{w}_{DD}.\end{aligned} \tag{3-145}$$

Similarly to the operations in the ZF algorithm, (3-145) can be simplified as

$$\mathbf{y}_{DD}^{ZF} = \left[\mathbf{H}_{DD}^{rect}(\mathbf{H}_{DD}^{rect})^H + \frac{1}{a}\mathbf{I}_{MN} \right]^{-1}(\mathbf{H}_{DD}^{rect})^H(\mathbf{H}_{DD}^{rect}\mathbf{x}_{DD} + \mathbf{w}_{DD}) \cdot \tag{3-146}$$

According to the matrix form of the DD domain input-output relation for rectangular pulses (3-118), we obtain

$$\mathbf{y}_{DD}^{ZF} = \left[\mathbf{H}_{DD}^{rect}(\mathbf{H}_{DD}^{rect})^H + \frac{1}{a}\mathbf{I}_{MN} \right]^{-1}(\mathbf{H}_{DD}^{rect})^H\mathbf{y}_{DD} \cdot \tag{3-147}$$

Due to the DD domain MMSE equalization matrix for rectangular pulses (3-137), we find (3-147) equivalent to (3-136), which means we have proved the equivalence of the ZF algorithm between time domain equalization and DD domain equalization for rectangular pulses.

3.5 Simulation Results and Analysis

In this section, we build the OTFS system in MATLAB and conducted simulations to study the bit error rate (BER) performance. The basic simulation parameters are shown in Table- 1.

Table- 1 Basic Simulation Parameters

Parameters	Symbols	Value
Number of paths	P	9
Number of carriers	M	64
Symbol duration	N	16
Carrier frequency	f_c	4 GHz
Carrier frequency spacing	Δf	15kHz

In the simulation, we use the LET-Extended Vehicular A (EVA) model as the wireless channel, whose delay taps are [0, 30, 150, 310, 370, 710, 1090, 1730, 2510]ns and power parameters are [0, -1.5, -1.4, -3.6, -0.6, -9.1, -7, -12, -16.9]dB, where the Doppler shift is randomly generated from zero to the maximum Doppler shift. In the following, we apply the ideal channel estimation and the MMSE equation at the receiver.

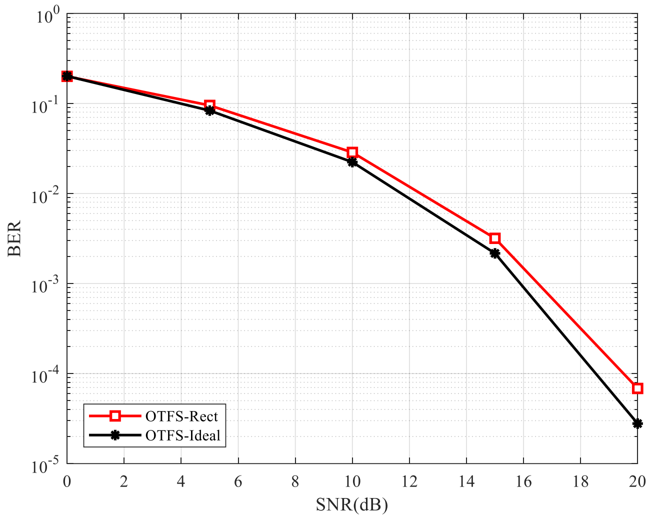

Figure 14 BER performances between ideal pulses and rectangular pulses.

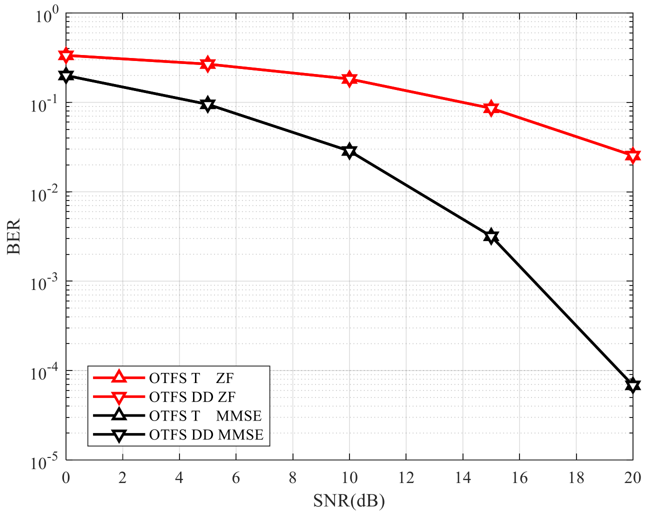

Figure 15 BER performances of equalizations in the T and DD domain.

Figure 14 shows that the BER performance of the rectangular waveform can approach that of the ideal waveform. Due to that the ideal waveform does not exist in practice, we can use the rectangular waveform to simply the OTFS system. Hence, we will use the rectangular pulse-shaping filter to generate the OTFS waveform in the following simulation.

Figure 15 verifies that the performances of ZF equalization in the T domain and the DD domain are exactly the same, as well as the MMSE equalization, which is consistent with our corresponding derivation in section 3.4.

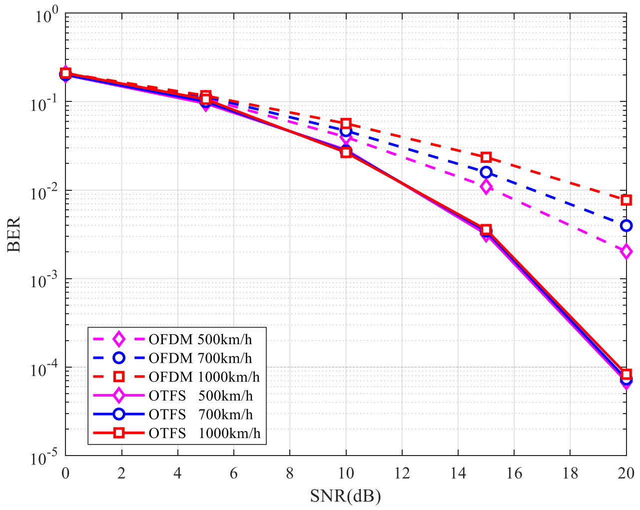

Figure 16 BER performances of OTFS compared with OFDM at different speeds.

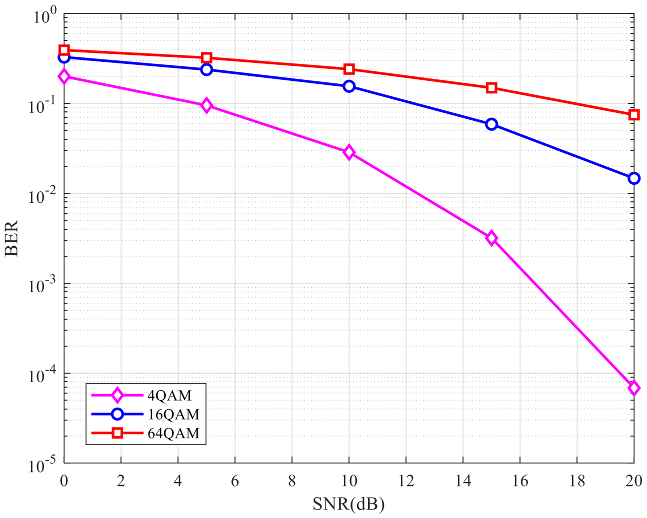

Figure 17 BER performances of OTFS with different orders of QAM.

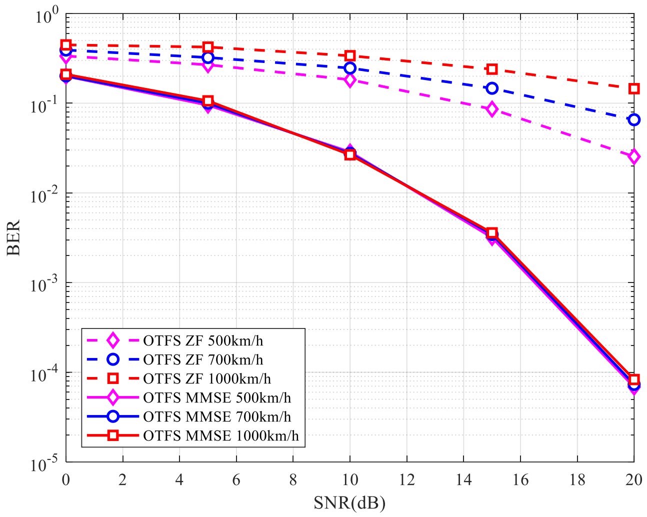

Figure 18 BER performances of ZF and MMSE equalization in the OTFS system.

Figure 16 compares the BER performances of the OTFS and OFDM at different speeds. The results indicate that as the speed increases, the performance of OFDM is significantly degraded, while OTFS exhibits superior performance. More specifically, at high speeds the BER performances of OTFS become even better than those at low low speeds and intend to converge to one curve, which indicates that OTFS exhibits excellent resilience to high Doppler shifts.

Figure 17 shows the BER performance of OTFS at 500km/h will decrease when the order of QAM modulation increases, which indicates that the OTFS system does not perform well under the condition of high-order IQ modulation.

Figure 18 demonstrates that the ZF equalization performance of OTFS is severely degraded with increasing speed, while the MMSE equalization does not, due to that the OTFS system is sensitive to the noise and ZF equalization is tended to amplify the noise in high SNR.

3.6 Summary of the Chapter

In this chapter, the principle and transmission scheme of the OTFS system are declared. Then, the reduced CP is introduced, which shows a better performance and increases the spectrum efficiency in the OTFS system, compared with the traditional full CP. The input-output relations are derived under various conditions in the different domains, as well as the effective matrix for different pulse-shaping filters. Moreover, the effect of ZF equalization in the time domain is proved to be identical to that in the DD domain, as well as the MMSE equalization, which has been verified by simulation.

Chapter Four Physical Layer Security in OTFS System

In this chapter, Wyner’s wire-tap channel model is introduced. Then, linear precoding methods, including ZF precoding, MMSE precoding, and SVD precoding are also indicated. Finally, a secure transmission scheme is researched to realize the PLS.

4.1 Wire-tap Channel Model

In recent years, physical layer security has become a research hotspot in the field of wireless communication, with rapid development. Physical layer security technology utilizes the diversity and time-varying nature of wireless channels, as well as the uniqueness and reciprocity of channel characteristics between communication terminals to implement secure transmission. It requires no key distribution but achieves fast access and high-strength security performance.

In 1975, Wyner from Bell Laboratories proposed the wire-tap channel model as shown in Figure 19. Wyner stated that achieving unconditional secure communication is feasible only when the wire-tap channel is worse than the legitimate channel (i.e. when the legitimate communicators possess an advantage in channel quality). This can be achieved through secure coding. Wyner's model presented a two-step approach to the realization of unconditional secrecy in communication systems. The first step involves establishing a wire-tap channel model where the legitimate users possess better channel conditions. The second step is to enhance the advantage of the legitimate receiver by secure coding[60].

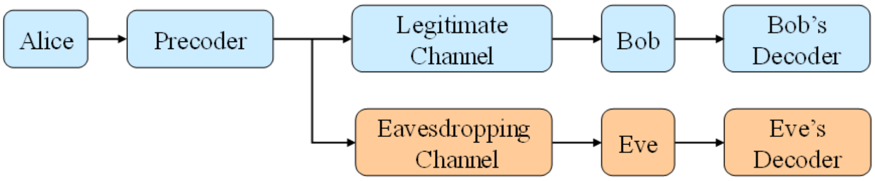

Figure 19 Wire-tap channel model.

4.2 Precoding Scheme

A precoding scheme refers to a technique used in communication systems to improve the reliability and efficiency of data transmission. It involves applying specific transformations or manipulations to the transmitted signal at the transmitter side before it is transmitted over the communication channel.

The primary objective of a precoding scheme is to mitigate the effects of channel impairments, such as noise, interference, and fading, and to enhance the quality of the received signal at the receiver side. By employing precoding, the transmitter can shape the transmitted signal to exploit the channel characteristics and maximize the received signal quality.

There are various types of precoding schemes used in different communication scenarios, including linear precoding, nonlinear precoding, and space-time precoding. Linear precoding techniques include ZF precoding, MMSE precoding, and SVD precoding, which aims to eliminate or reduce interference between users.

4.2.1 ZF Precoding

ZF precoding is one of the fundamental linear precoding techniques, whose purpose is to transmit signals to the intended user while simultaneously eliminating interference caused by other users. ZF precoding can be expressed as[61]

$$\mathbf{F}_{ZF} = \sqrt{\beta}\mathbf{H}^{H}(\mathbf{H}\mathbf{H}^{H})^{-1}, \tag{4-1}$$

where $\mathbf{H}\mathbf{H}^H$ is the Gram matrix. The gram matrix is also known as the inner product matrix, which is composed of vectors in a vector space. The elements of this matrix are obtained by calculating the inner products between the vectors, in which the off-diagonal elements represent interdependence while the diagonal elements represent the power difference.

In scenarios where no additive noise exists or when the additive noise is sufficiently small, ZF precoding is considered the optimal precoding scheme. However, when additive noise is present in the channel, ZF precoding has the drawback of amplifying the noise, leading to a significant impact on communication performance. When there are strong correlations between the channels, ZF precoding eliminates interference between the channels at the expense of sacrificing channel capacity[62].

4.2.2 MMSE Precoding

MMSE precoding is a precoding matrix designed to optimize the minimum mean square error of the desired data stream. The expression for MMSE precoding is given as follows

$$\mathbf{F}_{MMSE} = \sqrt{\beta}\mathbf{H}^H\left(\mathbf{H}\mathbf{H}^H + \alpha\mathbf{I}\right)^{-1}, \tag{4-2}$$

where α denotes the tuning parameter. When the signal-to-interference-plus-noise ratio (SINR) is relatively high α approaches zero, MMSE precoding does not consider the system noise but only suppresses interference between users, in which case the performance of MMSE precoding converges to ZF precoding. When the system noise is small, MMSE precoding mitigates the impact of noise on the communication system by sacrificing a portion of the performance, thereby enhancing channel capacity.

MMSE does not eliminate interference between users, however, it considers the impact of noise on the system, which finds an optimal trade-off between noise gain and residual interference. Therefore, MMSE precoding is more suitable than ZF precoding for various complex system environments.

4.2.3 SVD Precoding

SVD decomposition can transform the channel matrix into a Diagonal matrix to decomposite the channel into several mutually independent subchannels, which transforms the actual channel as equivalent to parallel orthogonal channels. Selecting subchannels with higher channel gains for signal transmission, not only reduces interference between data streams but also maximizes channel capacity.

The precoding method based on SVD has been adopted by the IEEE 802.11n wireless LAN standard[63]. SVD is a highly efficient method for handling matrix operations. Its effectiveness stems from the fact that any channel matrix, whether square or not, composed of either complex or real numbers, can be represented by SVD[64]

$$\mathbf{H} = \mathbf{U}\mathbf{\Lambda}\mathbf{V}^H , \tag{4-3}$$

where $\mathbf{\Lambda}$ denotes a diagonal matrix which contains diagonal elements composed of non-negative real numbers. $\mathbf{U}$ and $\mathbf{V}$ denote the unitary matrix composed of complex numbers, which satisfy

$$\mathbf{U}\mathbf{U}^H = \mathbf{U}^H\mathbf{U} = \mathbf{I} , \tag{4-4}$$

$$\mathbf{V}\mathbf{V}^H = \mathbf{V}^H\mathbf{V} = \mathbf{I} \cdot \tag{4-5}$$

The SVD decomposition is achieved through an iterative algorithm, where the maximum off-diagonal elements are eliminated using delay and Jacobi rotations. The decomposition transfers the channel energy onto the main diagonal, and it can be proven that this algorithm converges. However, due to the limited number of iterations and the order of the matrix, the result obtained is an approximation.

Assuming the transmitter knows the channel matrix $\mathbf{H}$, it can utilize the precoding matrix to encode the transmitted information by $\mathbf{x} = \mathbf{V}\mathbf{s}$. Hence the received signal can be represented by

$$\mathbf{y} = \mathbf{U}\boldsymbol{\Lambda}\mathbf{V}^{H}\mathbf{V}\mathbf{s} + \mathbf{n} = \mathbf{U}\boldsymbol{\Lambda}\mathbf{s} + \mathbf{n} \cdot \tag{4-6}$$

Assuming the receiver also knows the channel matrix $\mathbf{H}$, it can use the matrix $\mathbf{U}^{H}$ to decode the data at the receiver, and hence obtain

$$\mathbf{U}^{H}\mathbf{y} = \mathbf{U}^{H}\mathbf{U}\boldsymbol{\Lambda}\mathbf{s} + \mathbf{U}^{H}\mathbf{n}, \tag{4-7}$$

which can also be expressed as $\hat{\mathbf{y}} = \boldsymbol{\Lambda}\mathbf{s} + \hat{\mathbf{n}}$. This equation (4-7) implies that a system with interference channels can be transformed into multiple parallel channels that are mutually independent. The number of symbols that can be simultaneously transmitted over these parallel channels is determined by the rank of the channel matrix. The transmission quality of the channels is determined by the singular values.

Specifically, the channel matrix can be decomposed by $\mathbf{H} = \overline{\mathbf{U}}\boldsymbol{\Lambda}\overline{\mathbf{V}}^{H}$, hence the SVD precoder can be designed as $\mathbf{V} = \overline{\mathbf{V}}_{[1:r]}\mathbf{P}^{1/2}$, where $\mathbf{P} = (p_1, p_2, \dots, p_r)$ denotes the power allocation matrix. Therefore, the receiver filter can be designed as $\mathbf{U} = \overline{\mathbf{U}}_{[1:r]}$. Assuming that the receiver has known the channel matrix $\mathbf{H}$, it can process the received signal using the matrix $\mathbf{U}^{H}$ to obtain the received signal as

$$\mathbf{U}^{H}\mathbf{y} = \mathbf{U}^{H}\mathbf{H}\mathbf{V}\mathbf{s} + \mathbf{U}^{H}\mathbf{n}, \tag{4-8}$$

$$\hat{\mathbf{y}} = \mathbf{U}^{H}\mathbf{H}\mathbf{V}\mathbf{s} + \mathbf{U}^{H}\mathbf{n} \cdot \tag{4-9}$$

By selecting the singular vectors of the channel matrix as the precoders for the system, the maximum rate can be achieved by

$$R = log_2(|\ \mathbf{I} + \frac{\mathbf{P}}{k} R_{\mathbf{n}}^{-1}\mathbf{U}^H\mathbf{H}\mathbf{V}_{opt}\mathbf{V}_{opt}^H\mathbf{H}^H\mathbf{U}|)\,. \tag{4-10}$$

From (4-10), it can be observed that when $r = N_r$, $\mathbf{V}_{opt} = \mathbf{V}\mathbf{P}^{1/2}$ denotes the Optimal precoder.

4.3 SVD Secure Precoding in OTFS system

In the OTFS system, we intend to use the SVD precoding strategy to design a low-detection waveform to realize PLS, which is shown in Figure 20.

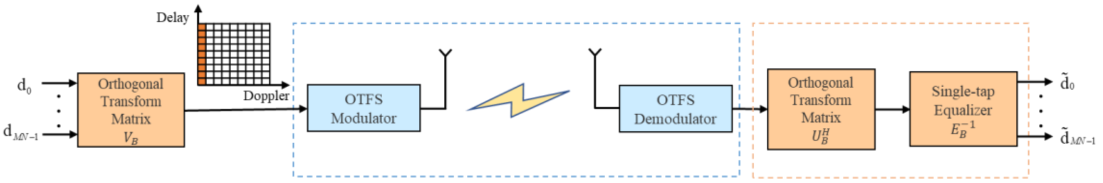

Figure 20 SVD secure precoding scheme in OTFS system.

At the transmitter, the source information of the OTFS system is a set of QAM symbols. These symbols are transmitted in a block size MN, which is also called an OTFS frame, which is denoted as

$$\mathbf{d} = [d_0, d_1, \cdots d_{MN-1}]^T \in \mathbb{C}^{MN\times 1}. \tag{4-11}$$

Then, the OTFS data block $\mathbf{d}$ will be preceded by an orthogonal transformation matrix $\mathbf{V}_B = [V_0, V_1, \cdots V_{MN-1}]^T \in \mathbb{C}^{MN\times MN}$, which is extracted from the effective channel matrix of the legitimate link in the DD domain

$$\mathbf{H}_B^{eff} = \mathbf{U}_B\mathbf{E}_B\mathbf{V}_B{}^H, \tag{4-12}$$

where $\mathbf{H}_B^{eff}$ denotes the effective channel matrix of the legitimate link in the DD domain, the left singular vector matrix $\mathbf{U}_B$ and the right singular vector matrix $\mathbf{V}_B^H$ are orthogonal matrices, and $\mathbf{E}_B$ is a diagonal matrix. The reason why we use the DD domain effective channel matrix to design the precoder is that the DD domain channel is more stable and sparse, and hence can be estimated by the stranded channel estimation[65], which also has been declared in section 2.3. Moreover, the reciprocal property of the wireless channel is used in our precoding strategy, where the downlink channel (the transmitter to the legitimate user) can be estimated from the uplink channel (the legitimate user to the transmitter) in a TDD or hybrid system[66].

SVD precoding is implemented by a linear matrix multiplication operation between the orthogonal transformation matrix $\mathbf{V}_B$ and the OTFS symbol vector $\mathbf{d}$, making the OTFS symbol block rotate in the DD domain

$$\mathbf{x} = \mathbf{V}_B \mathbf{d} \in \mathbb{C}^{MN \times 1} . \tag{4-13}$$

Then, the coded information $\mathbf{x}$ will go through the OTFS modulator and enter the open environment of the wireless channel. This process has been declared in section 3.1. There are eavesdroppers receiving the information from the wireless channel, as well as the legitimate user. From the matrix form of the input-output relation in the DD domain for rectangular pulses (3-118), both the legitimate user and eavesdroppers first process the data through the OTFS demodulator, and obtain the DD domain data by

$$\mathbf{y}_B = \mathbf{H}_B^{eff} \mathbf{x} + \mathbf{w}_B , \tag{4-14}$$

$$\mathbf{y}_E = \mathbf{H}_E^{eff} \mathbf{x} + \mathbf{w}_E , \tag{4-15}$$

where $\mathbf{y}_B$ and $\mathbf{y}_E$ denotes demodulated signal at the legitimate user and the eavesdroppers, respectively. From (3-119), $\mathbf{w}_B$ and $\mathbf{w}_E$ denotes the noise vector transformed into the DD domain.

At the legitimate receiver, the signal will be decoded by another orthogonal transformation matrix $\mathbf{U}_B^H$

$$\begin{aligned}\mathbf{y}_B &= \mathbf{U}_B^H \mathbf{y}_B \\ &= \mathbf{E}_B \mathbf{d} + \mathbf{U}_B^H \mathbf{w}_B\end{aligned}, \tag{4-16}$$

where we observe that the effect of $\mathbf{V}_B$ in the effective channel matrix decomposition is canceled by the precoding matrix $\mathbf{V}_B$. Also, the effect of $\mathbf{U}_B$ in the effective channel matrix decomposition is canceled by the decoding matrix $\mathbf{U}_B^H$. Hence, after decoding at the legitimate user, the precoding only leaves an effect caused by $\mathbf{E}_B$. Then, we apply a single-tap equalization designed by the diagonal matrix $\mathbf{E}_B^{-1}$, through which the legitimate user gets the equalized information symbols $\mathbf{d}_B$

$$\begin{aligned}\mathbf{d}_B &= \mathbf{E}_B^{-1} \mathbf{y}_B \\ &= \mathbf{d} + \mathbf{E}_B^{-1} \mathbf{U}_B^H \mathbf{w}_B\end{aligned}, \tag{4-17}$$

where the term $\mathbf{E}_B^{-1} \mathbf{U}_B^H \mathbf{w}_B$ is the effective noise term after decoding and equalization at the legitimate receiver.

Whereas at the eavesdropper, we consider the worst case, where the eavesdropper knows all the knowledge of the communication transmission scheme, including OTFS modulation technology and even our SVD precoding strategy. Once the signal is captured, it will be processed by OTFS demodulation and SVD decoding as

$$\begin{aligned}\mathbf{y}_E &= \mathbf{U}_E^H \mathbf{y}_E \\ &= \mathbf{E}_E \mathbf{V}_E{}^H \mathbf{V}_B \mathbf{d} + \mathbf{U}_E^H \mathbf{w}_E\end{aligned}. \tag{4-18}$$

Then, by the single-tap equalization $\mathbf{E}_E^{-1}$ at the eavesdropper, we obtain the equalized signal

$$\begin{aligned}\mathbf{d}_E &= \mathbf{E}_E^{-1} \mathbf{y}_E \\ &= \mathbf{V}_E{}^H \mathbf{V}_B \mathbf{d} + \mathbf{E}_E^{-1} \mathbf{U}_E^H \mathbf{w}_E\end{aligned}, \tag{4-19}$$

where we can observe that the eavesdroppers can not recover the original data symbols, for the effect of precoding by $\mathbf{V}_B$ can not be eliminated. Furthermore, even if they use the matrix $\mathbf{V}_E$ to cancel the effect of $\mathbf{V}_E{}^H$, and get $\mathbf{d}_E$

$$\begin{aligned}\mathbf{d}_E &= \mathbf{V}_E\mathbf{d}_E \\ &= \mathbf{V}_B\mathbf{d} + \mathbf{V}_E\mathbf{E}_E^{-1}\mathbf{U}_E^H\mathbf{w}_E\end{aligned}, \tag{4-20}$$

which is closer but still a degraded version of the original information $\mathbf{d}$. The term $\mathbf{V}_E\mathbf{E}_E^{-1}\mathbf{U}_E^H\mathbf{w}_E$ is the noise vector at the eavesdropper.

From (4-20), we know that the eavesdropper can only get the degraded version $\mathbf{d}_E$, which is still far from the original information $\mathbf{d}$, due to the difference between the legitimate channel and the eavesdropping channel. Furthermore, due to their unique physical positions, each channel in the physical channel is independent and distinct.

Therefore, by using our secure precoding strategy, only the legitimate user can decode the information correctly while the eavesdropper cannot. Even though we assume the eavesdropper is available to know all the knowledge of our transmission scheme, which realizes the physical layer security.

4.4 Simulation Results and Analysis

In this section, we build an R-OTFS system in MATLAB for simulation. The system parameters and channel model used are the same as those described in Chapter 3 for the OTFS system.

We first analyze the statistical characteristics of the received signal at the eavesdroppers under 500km/h. Figure 21(a) shows that the envelope of the eavesdropper's received signal amplitude approximately follows a Rayleigh distribution with a variance of 0.9. Figure 21(b) indicates that the phases of the eavesdropper's received signal follow a uniform distribution within the range $[-\pi, \pi]$.

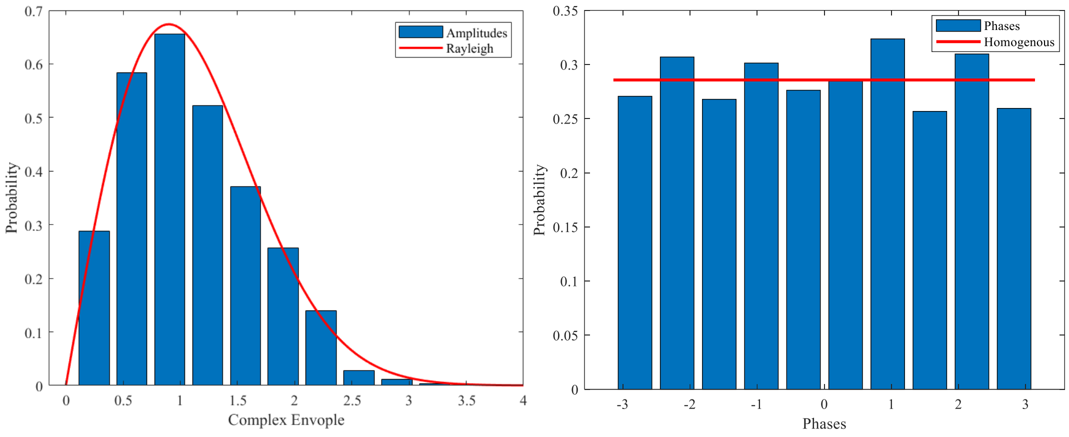

(a) Statistic of Amplitudes (b) Statistic of Phases

Figure 21 Statistics of R-OTFS signal's amplitudes and phases.

Through the distribution of the amplitudes and phases at eavesdroppers in Figure 21, it can be observed that the information encoded by SVD secure precoding strategy appears as noise to the eavesdroppers, thereby reducing the interception probability.

Next, we analyze the BER performance of the R-OTFS transmission scheme under 700km/h. From Figure 22, it can be observed that our R-OTFS single-tap equalization scheme exhibits better BER performance than ZF at high speeds, although slightly inferior to MMSE equalization. However, under low SNR conditions, our proposed R-OTFS achieves BER performance much close to OTFS with MMSE equalization. Furthermore, we observe when SNR in dB increases linearly, the BER curve of R-OTFS exhibits an almost linear declining trend.

Moreover, to ensure that our proposed R-OTFS waveform generated by the SVD secure precoding can retain its ability to resist the high Doppler effect similar to the normal OTFS system, we show the BER performance of the R-OTFS system in Figure 23, which indicates that our R-OTFS waveform maintains a superior performance barely not affected by the high speed.

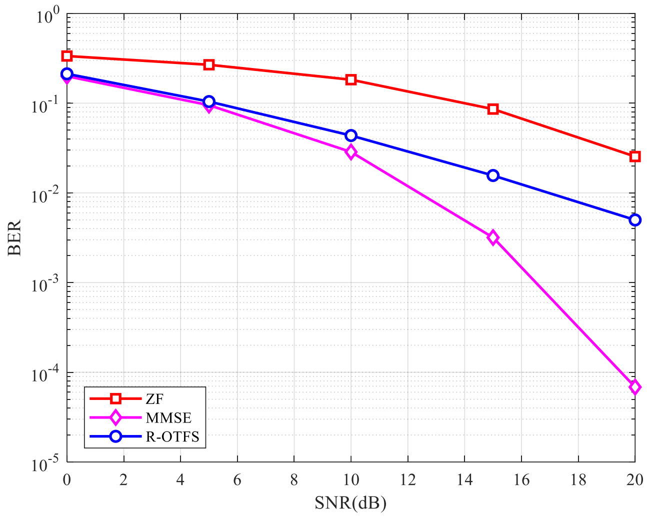

Figure 22 BER performances of R-OTFS compared with OTFS.

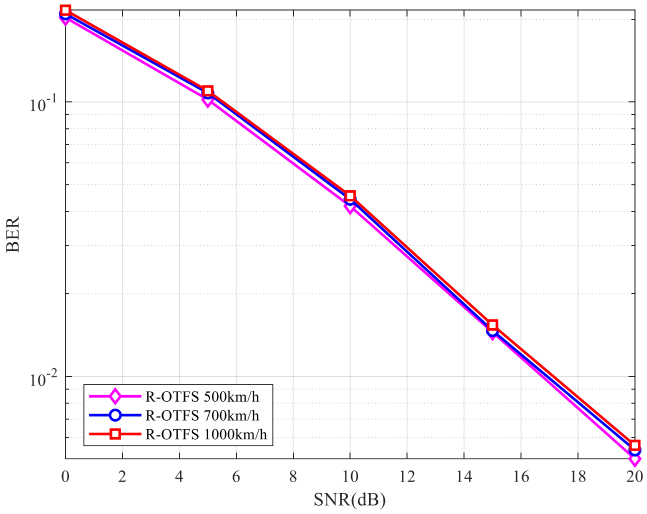

Figure 23 BER performance of R-OTFS at different speeds.

Finally, we analyze the BER as well as the security performance of the received signals for legitimate users and eavesdroppers. We classify eavesdroppers into three distinct levels: Eve1, who is aware of the OTFS modulation scheme but lacks knowledge of the SVD secure precoding; Eve2, who possesses knowledge of the SVD precoding scheme and attempts to decode the signals using the eavesdropping channel; and Eve3, who is even more sophisticated, possessing knowledge of both the R-OTFS modulation scheme and employing the precoding matrix $\mathbf{V}_E$ to mitigate the effects of $\mathbf{V}_E^H$. Figure 24 demonstrates that in our R-OTFS secure transmission, all levels of eavesdroppers exhibit a steady BER of 0.5, rendering them unable to accurately decode the information even when equipped with comprehensive prior knowledge. However, only the legitimate user can correctly decode the information without being affected by precoding rotation or high Doppler.

Additionally, we provide the constellation diagrams of the legitimate user and eavesdroppers as shown in Figure 25. It can be inferred that the constellation diagrams for all levels of eavesdroppers approximately obey the Gaussian distributions, indicating that even the most sophisticated eavesdropper can only obtain the degraded version of the information.

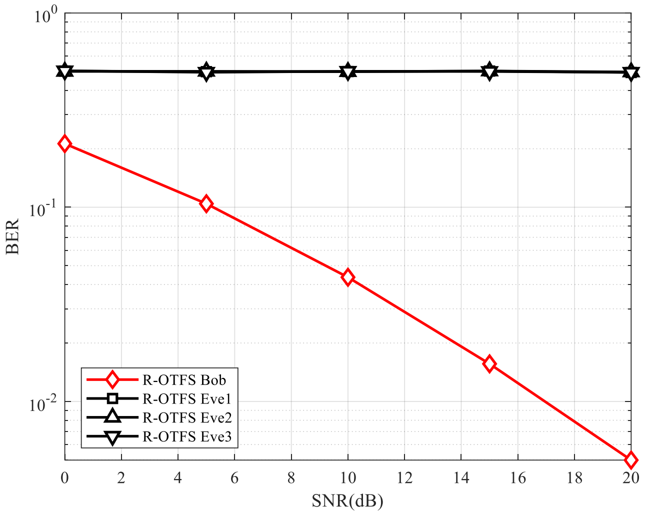

Figure 24 BER performances of R-OTFS between Bob and Eves.

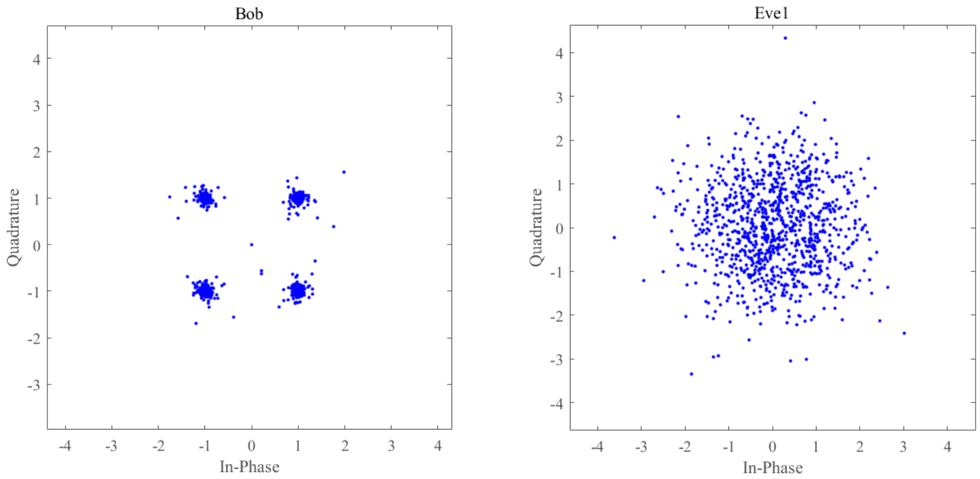

(a) Bob

(b) Eve1

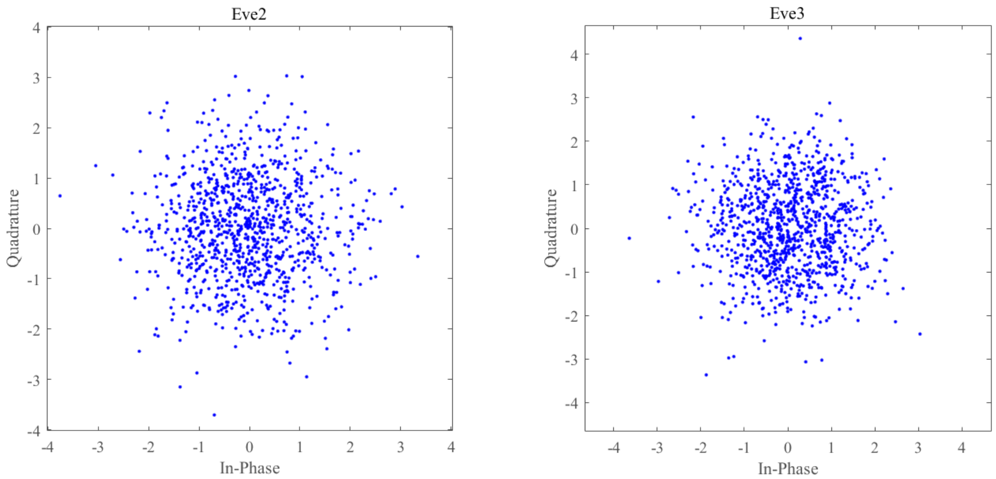

(c) Eve2 (d) Eve3

Figure 25 Constellations of Bob and Eves.

4.5 Summary of the Chapter

In this chapter, the wire-tap model in the physical layer security is indicated. Then, three commonly used linear precoding methods are introduced, which are ZF precoding, MMSE precoding, and SVD precoding. Finally, an SVD secure precoding strategy is researched to generate the R-OTFS waveform, which rotates the information symbols and distorts the constellation at the eavesdropper. Even if the eavesdroppers are assumed to know everything about the R-OTFS transmission scheme, still they cannot recover the original information but a degraded version, which realizes the physical layer security in high-mobility communication scenarios.

Chapter Five Summary and Prospect

5.1 Summary

This thesis studies the physical layer security based on the OTFS system. Firstly, the transmission characteristics and representations of the wireless channel are studied, then the physical discrete-path model is built. Secondly, the principle and the transmission scheme of the orthogonal time frequency space modulation are also introduced. Subsequently, the input-output relations in different domains are analyzed based on various types of interference in the received signal. Finally, from the perspective of physical layer security, a secure precoding strategy is researched to generate a low-interception waveform in the OTFS system. The main contents and achievements of this thesis are summarized as follows:

1) The OTFS system is introduced, which exhibits superior performance compared to traditional OFDM technology, especially in high-speed scenarios where subcarriers are severely degraded. The simulation results show that the OTFS system demonstrates excellent performance and robustness in high-mobility 6G wireless communication scenarios, particularly in terms of high Doppler tolerance.

2) The input-output relationships of OTFS are derived in various conditions and forms, based on which the inter-carrier interference, inter-symbol interference, and inter-delay interference are analyzed. Subsequently, the equivalent matrix expressions for different domains are derived, considering the use of arbitrary pulse shaping and practical rectangular pulse shaping. Moreover, the effect of ZF equalization in the time domain is proved to be identical to that in the DD domain, as well as the MMSE

equalization, which has been verified by our simulation results.

3) A secure precoding strategy is studied based on the OTFS system. Leveraging the unique characteristics of the physical channel, an SVD precoding technique is applied to rotate the information symbols in the DD domain based on the channel. The R-OTFS waveform only enables the legitimate user to decode correctly, while introducing rotational distortion in the constellation diagram received by eavesdroppers. Even if eavesdroppers have knowledge of the transmission mechanism and SVD precoding, they can only obtain degraded information, thus achieving physical layer security.

5.2 Prospect

In this thesis, the principle of OTFS are studied and the input-output relationships are derived in various conditions. Based on the OTFS system, an SVD-based secure precoding strategy is applied to achieve physical layer security. However, there are still limitations in the work conducted, and improvements should be made in future research:

1) In this thesis, the OTFS secure precoding system is assumed using the ideal channel estimation in a TDD system. However, in practical high-speed scenarios, channel estimation may not achieve ideal performance. In future research, further investigation will be conducted on channel estimation techniques for OTFS in high-mobility scenarios.

2) The present thesis focuses on the SISO-OTFS system, but SVD precoding is a commonly used precoding method in large-scale MIMO systems. Therefore, considering the potential of this secure precoding technique in MIMO scenarios, the

transmission security in multi-user scenarios by applying the massive MIMO technology should be focused in future research.

Reference

[1] Feng Y., Zhang W., Ge Y., et al. channel time-variation suppression with optimized receive beamforming for high-mobility OFDM downlink transmissions[J]. IEEE Transactions on Communications, 2022, 70(2): 1183-1196.

[2] Fozi M., Sharafat A. R., and Bennis M. Fast mimo beamforming via deep reinforcement learning for high mobility mmWave connectivity[J]. IEEE Journal on Selected Areas in Communications, 2022, 40(1): 127-142.

[3] Huang Z., Zheng B., and Zhang R. Transforming fading channel from fast to slow: IRS-assisted high-mobility communication[C]. 2021 IEEE International Conference on Communications (ICC), 2021: 1-6.

[4] Guo W., Zhang W., Mu P., et al. High-mobility wideband massive MIMO communications: Doppler compensation, analysis and scaling laws[J]. IEEE Transactions on Wireless Communications, 2019, 18(6): 3177-3191.

[5] Zhou Y. and Ai B. Provide high-QoS of the high-speed railway mobile communications in cyber-physical systems[J]. Computer science, 2014.

[6] Hou X., Ling J., and Wang D. Performance of high-mobility MIMO communications with Doppler diversity[J]. IEEE Access, 2020, 8: 31574-31585.

[7] Monk A., Hadani R., Tsatsanis M., et al. OTFS-orthogonal time frequency space: A novel modulation technique meeting 5G high mobility and massive MIMO challenges[J]. arXiv preprint arXiv, 2016, 9: 1608.

[8] Sun Y., Wang C., Cai H., et al. Deep learning based equalizer for MIMO-OFDM systems with insufficient Cyclic Prefix[C]. 2020 IEEE 92nd Vehicular Technology

Conference (VTC2020-Fall). IEEE, 2020: 1-5.

[9] Li J. Research on key technologies of orthogonal time frequency space transmission in fast time varing fading channels[D]. University of Electronic Science and Technology of Chinal. 2022.

[10] Hadani R., Rakib S., Tsatsanis M., et al. Orthogonal Time Frequency Space Modulation[C]. 2017 IEEE Wireless Communications and Networking Conference (WCNC), 2017: 1-6.

[11] Wang D., Sun B., Wang F., et al. Transmit diversity scheme design for rectangular pulse shaping based OTFS[J]. China Communications, 2022, 19(3): 116-128.

[12] Huang Z., Cao S., Wei H., et al. Research on channel estimation algorithm based on OTFS system[C]. 2022 IEEE 6th Information Technology and Mechatronics Engineering Conference (ITOEC). IEEE, 2022, 6: 352-356.

[13] Ma Y., Ma G., Wang N., et al. OTFS-TSMA for massive internet of things in high-speed railway[J]. IEEE Transactions on Wireless Communications, 2022, 21(1): 519-531.

[14] Shin W., Kim K., and Ko Y. J. Performance comparison of equalization schemes for OTFS over time-varying multipath channels[C]. 2020 International Conference on Information and Communication Technology Convergence (ICTC). IEEE, 2020: 1433-1438.

[15] Bhat V. S., Dayanand S. G., and Chockalingam A. Performance analysis of OTFS modulation with receive antenna selection[J]. IEEE Transactions on Vehicular Technology, 2021, 70(4): 3382-3395.

[16] Liu F., Yuan Z., Guo Q., et al. Message passing based structured sparse signal recovery for estimation of OTFS channels with fractional Doppler shifts[J]. IEEE Transactions on Wireless Communications, 2021.

[17] Mukherjee A., Fakoorian S. A. A., Huang J., et al, Principles of physical layer security in multiuser wireless networks: A survey[J]. IEEE Communications Surveys & Tutorials, 2014, 16(3): 1550-1573.

[18] Bloch M. and Barros J. Physical-layer security: From information theory to security engineering[M]. 2011.

[19] Hadani R., Rakib S., Molisch A. F., et al. Orthogonal time frequency space (OTFS) modulation for millimeter wave communications systems[C]. 2017 IEEE/MTT-S International Microwave Symposium (IMS), 2017.

[20] Raviteja P., Phan K. T., Hong Y., et al. Interference cancellation and iterative detection for orthogonal time frequency space modulation[J]. IEEE Transactions on Wireless Communications, 2018:6501-6515.

[21] Li L., Liang Y., Fan P., et al. Low complexity detection algorithms for OTFS under Rapidly time-varying channel[C]. 2019 IEEE 89th Vehicular Technology Conference (VTC2019-Spring), 2019.

[22] Zhao J. Research on signal detection technology in OTFS communication system[D]. Nanjing University of Posts and Telecommunications, 2022.

[23] Qu H., Liu G., Zhang L., et al. Low-complexity symbol detection and interference cancellation for OTFS system[J]. IEEE Transactions on Communications, 2020: 99.

[24] Ding Z., Schober R., Fan P., et al. OTFS-NOMA: An efficient approach for exploiting heterogenous user mobility profiles[J]. IEEE Transactions on Communications, 2019.

[25] Li S., Yuan W., Wei Z., et al. Cross domain iterative detection for orthogonal time frequency space modulation[J]. 2021.

[26] Ramachandran M. K. and Chockalingam A. MIMO-OTFS in high-doppler fading channels: signal detection and channel estimation[J]. IEEE, 2018.

[27] Murali K. R. and Chockalingam A. On OTFS modulation for high-Doppler fading channels[J]. IEEE Transactions on Wireless Communications, 2018:1-10.

[28] Liu X. Precoding and detection for orthogonal time frequency space signal under high-mobility scenarios[D]. Southwest Jiaotong University, 2021.

[29] Xie Y. Research on MIMO-OTFS index modulation[D]. Huazhong University of Science & Technology, 2021.

[30] Wang J. Research on DD domain grid resource allocation and spectrum efficiency for uplink of OTFS system[D]. Nanjing University of Posts and Telecommunications, 2022.

[31] Zhang X., Guo D., and Guo K. Secure performance analysis for multi-pair AF relaying massive MIMO systems in Ricean channels[J]. IEEE Access. 2018, 6:57708–57720.

[32] Yuan X. and Zhu J. Physical layer security throughput optimization scheme CombateMultiple eavesdroppers in time reversal system[J]. Journal of Signal Processing, 2021, 37(3): 437-446.

[33] Sadeghzadeh M., Maleki M., Salehi M., et al. Large-scale analysis of physical-layer security in multi-user wireless networks[J]. IEEE Transactions on Communications, 2018, 66(12): 6450-6462.

[34] Hong Y., Jing X., and Gao H. Programmable weight phased-array transmission for secure millimeter-wave wireless communications[J]. IEEE Journal of Selected Topics in Signal Processing. 2018, 12(2): 399–413.

[35] Ma R., Yang W., Sun X., et al. Secure communication in millimeter wave relaying networks[J]. IEEE Access. 2019, 7:31218–31232.

[36] Cheng F., Gui G., Zhao N., et al. UAV-relaying-assisted secure transmission with caching[J]. IEEE Transactions on Communications. 2019, 67(5):3140–3153.

[37] Zhou Y., Pan C., Yeoh P. L., et al. Secure communications for UAV-enabled mobile edge computing systems[J]. IEEE Transactions on Communications. 2020, 68(1):376–388.

[38] Chen X., Yang Z., Zhao N., et al. Secure transmission via power allocation in NOMA-UAV networks with circular trajectory[J]. IEEE Transactions on Vehicular Technology. 2020, 69(9):10033–10045.

[39] Xiao L., Xu Y., Yang D., et al. Secrecy energy efficiency maximization for UAV-enabled mobile relaying[J]. IEEE Transactions on Green Communications and Networking, 2020, 4(1): 180-193.

[40] Zhang J., Wu F., Zhu Y., et al. Joint trajectory and power optimization for mobile jammer-aided secure UAV relay network [J]. IEEE Transactions on Vehicular Communications, 2021, 30(4): 100357.

[41] Cui M., Zhang G., Wu Q., et al. Robust trajectory and transmit power design for secure UAV communications [J]. IEEE Transactions on Vehicular Technology, 2018, 67(9): 9042-9046.

[42] Sun X., Yang W., Cai Y., et al. Secure mmWave UAV-enabled swipt networks based on random frequency diverse arrays [J]. IEEE Internet of Things Journal, 2021, 8(1): 528-540.

[43] Liu M. Research on OTFS signal processing technologies based on deep learning [D]. Zhejiang University, 2022.

[44] klar B, Harris F J. Digital communications: Fundamentals and applications[M]. Englewood Cliffs: Prentice hall, 1988.

[45] Cho Y., Kim J., Yang W., et al. MIMOOFDM wireless communications with MATLAB[M]. Hoboken: John Wiley & Sons, 2010.

[46] Liu T. On Pilot Sequence Design and Channel Estimation in OTFS System [D]. Southwest Jiaotong University, 2019.

[47] Wang L. Research on power allocation in OTFS-NOMA cross-domain transmission system [D]. Nanjing University of Posts and Telecommunications, 2021.

[48] Liu X. Precoding and detection for orthogonal time frequency space signal under high-mobility scenarios [D]. Southwest Jiaotong University, 2021.

[49] Andrea Goldsmith. Wireless communications[M]. Posts & Telecom Press, 2007: 23-44.

[50] Li L. Performance analysis and optimizition of Doppler resilient orthogonal time

frequency space system[D]. Southwest Jiaotong University, 2019.

[51] Bello P. Characterization of randomly time-variant linear channels[J]. IEEE Transactions on Communications Systems, 1963, 11(4): 360-393.

[52] Liu C. Research on mmWave automotive integrated radar and communication technology based on OTFS modulation[D]. Southeast University, 2016.

[53] Xie Y. Research on MIMO-OTFS with index modulation[D]. Huazhong University of Science & Technology, 2021.

[54] Wang J. Research on DD domain grid resource allocation and spectrum efficiency for uplink of OTFS system[D]. Nanjing University of Posts and Telecommunications, 2022.

[55] Sayeed A. M., Sivanadyan T., Liu K., et al. Wireless communication and sensing in multipath environments using multi-antenna transceivers in handbook on array processing and sensor networks[M]. IEEE Press, 2010: 3-7.

[56] RezazadehReyhani A., Farhang A., Ji M., et al. Analysis of discrete-time MIMO OFDM-based orthogonal time frequency space modulation[C]. 2018 IEEE International Conference on Communications(ICC), 2018:1-6.

[57] Farhang A., RezazadehReyhani A., Doyle L. E., et al. low complexity modem structure for OFDM-based orthogonal time frequency space modulation[J]. IEEE Wireless Communications Letters, 2018, 7(3): 344-347.

[58] Raviteja P., Hong Y., Viterbo E., et al. Practical pulse-shaping waveforms for reduced-cyclic-prefix OTFS[J]. IEEE Transactions on Vehicular Technology, 2019, 68(1): 957-961.

[59] Wei Z., Yuan W., Li S., et al. Transmitter and receiver window designs for orthogonal time-frequency space modulation[J]. IEEE Transactions on Communications, 2021, 69(4): 2207-2223.

[60] Wyner A. D. The wire-tap channel［J］. Bell System Technical Journal, 1975, 54(8): 1355-1387.

[61] He H., Wen C., Jin S., et al. A model-driven deep learning network for MIMO detection[C]. 2018 IEEE Global Conference on Signal and Information Processing (GlobalSIP), 2018: 584-588.

[62] He X. Research on hybrid precoding technology in milimeter-wave massive MIMO systems [D].Guilin University of Electronic Technology, 2020.

[63] Perahia E. and Stacey R. Next generation wireless LANs: Throughput, robustness, and reliability in 802.11n[M]. Cambridge University Press, 2008.

[64] Cui W. MIMO Precoding Methods Based on Deep Learning [D]. Qilu University of Technology, 2021.

[65] Suraj S., Rahul K., Aditya K., et al. Bayesian learning aided sparse channel estimation for orthogonal time frequency space modulated systems[J]. IEEE Transactions on Vehicular Technology, 2021, 70(8): 8343–8348.

[66] Sun J., Wang Z., and Huang Q. Secure precoded orthogonal time frequency space modulation[C]. 2021 13th International Conference on Wireless Communications and Signal Processing (WCSP), 2021: 1-5.

Acknowledgement

First of all, I would like to give my heartfelt thanks to all the people who have ever helped me with this thesis.

My sincere and hearty thanks and appreciations go firstly to my supervisor, Professor Xu Qian, whose suggestions and encouragement have given me much insight into these translation studies. It has been a great privilege and joy to study under her guidance and supervision.

Also, I want to express my appreciation to all teachers such as Professor Yang Xin, Sun Wenbin, Wang Dawei, Gong Yanyun, and Wang Ling, who have lectured me with their insightful opinions which are of great benefit to me in my research. Besides, I shall show my appreciation to my head teacher Professor Zuo Xiaoya and my student mentor Professor Zhao Honggang for their attentive guidance for my graduation.

Especially, this thesis owes a debt to Huang Jiansong, as well as my other fellow grad students, such as Duan Zhengxiang, Cheng Pan, Mao Yaqi, You Qian, Zhou Ruizhe, Zhou Hanyu, Liu Ting, Liu Qianhui, and Zhao Lei, who have kindly provided me with assistance and companionship in the course of preparing this thesis.

In addition, my acknowledgement also goes to my roommates, Jiang Xiao, Ji Zekai, and Fan Minghao, as well as my classmates in the international class, who have helped me in both study and life. Moreover, many thanks go to my family for their unfailing love and unwavering support.

Finally, I am grateful to all those who devote much time to reading this thesis and giving me much advice, which will benefit me in my later study.

Appendix A

The proof of the input-output relation in the TF domain in matrix form is given as follows

$$\begin{aligned}
\mathbf{y}_{TF} &= vec(\mathbf{Y}_{TF}) \\
&= vec(\mathbf{F}_M \mathbf{G}_{rx} \mathbf{R}_T) \\
&= (\mathbf{I}_N \otimes \mathbf{F}_M \mathbf{G}_{rx}) vec(\mathbf{R}_T) \\
&= (\mathbf{I}_N \otimes \mathbf{F}_M \mathbf{G}_{rx}) \mathbf{r}_T \\
&= (\mathbf{I}_N \otimes \mathbf{F}_M \mathbf{G}_{rx})(\mathbf{H}_T \mathbf{s}_T + \mathbf{w}_T) \\
&= (\mathbf{I}_N \otimes \mathbf{F}_M \mathbf{G}_{rx}) \mathbf{H}_T \mathbf{s}_T + (\mathbf{I}_N \otimes \mathbf{F}_M \mathbf{G}_{rx}) \mathbf{w}_T \\
&= (\mathbf{I}_N \otimes \mathbf{F}_M \mathbf{G}_{rx}) \mathbf{H}_T vec(\boldsymbol{S}_T) + (\mathbf{I}_N \otimes \mathbf{F}_M \mathbf{G}_{rx}) \mathbf{w}_T \\
&= (\mathbf{I}_N \otimes \mathbf{F}_M \mathbf{G}_{rx}) \mathbf{H}_T vec(\mathbf{G}_{tx} \mathbf{F}_M^H \mathbf{X}_{TF}) + (\mathbf{I}_N \otimes \mathbf{F}_M \mathbf{G}_{rx}) \mathbf{w}_T \\
&= (\mathbf{I}_N \otimes \mathbf{F}_M \mathbf{G}_{rx}) \mathbf{H}_T (\mathbf{I}_N \otimes \mathbf{G}_{tx} \mathbf{F}_M^H) vec(\mathbf{X}_{TF}) + (\mathbf{I}_N \otimes \mathbf{F}_M \mathbf{G}_{rx}) \mathbf{w}_T \\
&= (\mathbf{I}_N \otimes \mathbf{F}_M \mathbf{G}_{rx}) \mathbf{H}_T (\mathbf{I}_N \otimes \mathbf{G}_{tx} \mathbf{F}_M^H) \mathbf{x}_{TF} + (\mathbf{I}_N \otimes \mathbf{F}_M \mathbf{G}_{rx}) \mathbf{w}_T \\
&= \mathbf{H}_{TF} \mathbf{x}_{TF} + \mathbf{w}_{TF} \ .
\end{aligned}$$

Appendix B

The proof of the input-output relation in the DD domain in matrix form is given as follows

$$\begin{aligned}
\mathbf{Y}_{DD} &= \mathbf{F}_M^H \mathbf{Y}_{TF} \mathbf{F}_N = \mathbf{F}_M^H (\mathbf{F}_M \mathbf{G}_{rx} \mathbf{R}_T) \mathbf{F}_N = \mathbf{G}_{rx} \mathbf{R}_T \mathbf{F}_N \\
\mathbf{y}_{DD} &= vec(\mathbf{Y}_{DD}) \\
&= vec(\mathbf{G}_{rx} \mathbf{R}_T \mathbf{F}_N) \\
&= (\mathbf{F}_N^T \otimes \mathbf{G}_{rx}) vec(\mathbf{R}_T) \\
&= (\mathbf{F}_N \otimes \mathbf{G}_{rx}) \mathbf{r}_T \\
&= (\mathbf{F}_N \otimes \mathbf{G}_{rx})(\mathbf{H}_T \mathbf{s}_T + \mathbf{w}_T) \\
&= (\mathbf{F}_N \otimes \mathbf{G}_{rx}) \mathbf{H}_T vec(\boldsymbol{S}_T) + (\mathbf{F}_N \otimes \mathbf{G}_{rx}) \mathbf{w}_T \\
&= (\mathbf{F}_N \otimes \mathbf{G}_{rx}) \mathbf{H}_T vec(\mathbf{G}_{tx} \mathbf{X}_{DD} \mathbf{F}_N^H) + (\mathbf{F}_N \otimes \mathbf{G}_{rx}) \mathbf{w}_T \\
&= (\mathbf{F}_N \otimes \mathbf{G}_{rx}) \mathbf{H}_T (\mathbf{F}_N^H \otimes \mathbf{G}_{tx}) vec(\mathbf{X}_{DD}) + (\mathbf{F}_N \otimes \mathbf{G}_{rx}) \mathbf{w}_T \\
&= (\mathbf{F}_N \otimes \mathbf{G}_{rx}) \mathbf{H}_T (\mathbf{F}_N^H \otimes \mathbf{G}_{tx}) \mathbf{x}_{DD} + (\mathbf{F}_N \otimes \mathbf{G}_{rx}) \mathbf{w}_T \\
&= \mathbf{H}_{DD} \mathbf{x}_{DD} + \mathbf{w}_{DD} \ .
\end{aligned}$$